

Evidence for Strongly Correlated Superconductivity in $\text{La}_3\text{Ni}_2\text{O}_7$ from First Principles

Daan Verraes,^{1,2} Tom Braeckvelt,¹ Nick Bultinck,^{2,*} and Veronique Van Speybroeck^{1,†}

¹Center for Molecular Modeling, Ghent University, Technologiepark 46, 9052 Zwijnaarde, Belgium

²Department of Physics and Astronomy, Ghent University, Krijgslaan 281, 9000 Ghent, Belgium

We conduct first-principles simulations of pressurized $\text{La}_3\text{Ni}_2\text{O}_7$, a material in which a recent series of experiments has found signs of high-temperature superconductivity. In the pressure range where superconductivity is observed, we find a significant increase in the Hubbard U parameter (*i.e.*, the strength of on-site repulsion) for the maximally localized Wannier states comprising the density functional theory (DFT) bands crossing the Fermi energy. We attribute this increase in U to reduced screening by the nearby La $5d$ bands – an effect that is sensitive to the pressure-driven crystal structure. Our results therefore indicate that the superconducting region in the $\text{La}_3\text{Ni}_2\text{O}_7$ phase diagram coincides with a region of enhanced electronic correlations. *Ab initio* molecular dynamics simulations extend these trends to finite temperatures, providing insights into the experimentally observed transition lines. Finally, we explore intrinsic chemical pressure using DFT simulations of $\text{Ac}_3\text{Ni}_2\text{O}_7$.

I. INTRODUCTION

Nearly four decades after the experimental discovery of high-transition-temperature (high- T_c) superconductivity in hole-doped cuprates, many features of the intricate strongly-coupled phase diagrams of these materials remain poorly understood [1–3]. To further expand the field of strong-coupling superconductivity, the closely related nickel-based oxides (featuring a Ni^+ configuration isoelectronic to the Cu^{2+} cations in cuprates) were proposed as promising candidate-high- T_c materials [4–6]. In particular, the parent Ruddlesden-Popper (RP) nickelates $R_{n+1}\text{Ni}_n\text{O}_{3n+1}$ and their reduced, infinite-layer (IL) series $R_{n+1}\text{Ni}_n\text{O}_{2n+2}$ have been the subject of intense investigation [7–11]. Superconductivity in nickelates was finally observed in 2019, in thin films of $\text{Nd}_{1-x}\text{Sr}_x\text{NiO}_2$ [12]. Subsequent works observed superconductivity in other IL nickelates, though exclusively in thin films, achieving a maximum T_c of 31 K – still significantly lower than most cuprates [13–15].

In a experimental breakthrough superconductivity was observed in bulk samples of the $n = 2$ RP nickelate $\text{La}_3\text{Ni}_2\text{O}_7$ at applied pressures above 14 GPa [16, 17]. Transport measurements proposed a right-triangle shaped superconducting region in the temperature-pressure phase diagram between 14 and 90 GPa, with a maximum T_c of 83 K at 18 GPa [18]. These experiments have thus identified the (non-IL) RP nickelates as a new class of bulk superconductors with T_c exceeding the boiling point of liquid nitrogen. The structural and electronic differences with the cuprates have motivated a plethora of theoretical works to unmask the pairing mechanism at play in $\text{La}_3\text{Ni}_2\text{O}_7$ [19–50].

As a member of the RP nickelates, the conventional polymorph of $\text{La}_3\text{Ni}_2\text{O}_7$ features intact bilayers of NiO_6 octahedra (Fig. 1(a)), with a formal nickel oxidation of

$\text{Ni}^{2.5+}$ ($3d^{7.5}$) [51]. This hole concentration level suggests a multi-orbital low-energy configuration, which is significantly different from that of the Ni^+ ($3d^9$) cations forming the square-planar NiO_2 layers in IL nickelates, or the Cu^{2+} ($3d^9$) cations in the CuO_2 planes of the cuprate materials. Density functional theory (DFT) calculations within the generalized gradient approximation suggest that the electron density near the Fermi energy is comprised mostly of the Jahn-Teller distorted e_g orbitals, which exhibit hybridization with adjacent O $2p$ orbitals along their symmetry-aligned axes [19–21]. DFT band structures suggest a physical picture in which the active Ni d_{z^2} orbitals form strong σ -bonds with the apical O p_z orbitals connecting the bilayers, giving rise to a large interlayer hopping which splits the d_{z^2} orbitals into bonding and antibonding states. The $d_{x^2-y^2}$ orbitals, on the other hand, remain approximately decoupled between different layers. This orbital-selective (2Ni)⁵⁺ configuration, shown in Fig. 1(b), suggests the construction of an effective dimer model from the four orbitals (the d_{z^2} and $d_{x^2-y^2}$ orbitals in each layer) which make up most of the DFT bands near the Fermi energy in $\text{La}_3\text{Ni}_2\text{O}_7$. Based on these first-principles considerations many bilayer Hubbard and t - J models have been proposed and studied in the literature, with a particular emphasis on stabilizing superconductivity [20–39].

On the experimental side, the crystal structure of $\text{La}_3\text{Ni}_2\text{O}_7$ at superconducting conditions is not yet completely resolved due to resolution constraints in the reported X-ray diffraction (XRD) data. At room temperature, the bilayer polymorph of $\text{La}_3\text{Ni}_2\text{O}_7$ encounters a first-order structural transition between two orthorhombic ($a \neq b$) phases, symmetrizing from space group $Cmcm$ to subgroup $Fmmm$ above a critical pressure of 14 GPa [16]. One of the most noteworthy geometric changes at this transition is the alignment of the NiO_6 octahedra along the c -axis as depicted in Fig. 1(c). DFT calculations find that this octahedral alignment coincides with a metallization of the σ -bonding states, which has been suggested to stabilize the observed superconductivity at low temperatures [52]. Subsequent synchrotron

* Contact author: Nick.Bultinck@UGent.be

† Contact author: Veronique.VanSpeybroeck@UGent.be

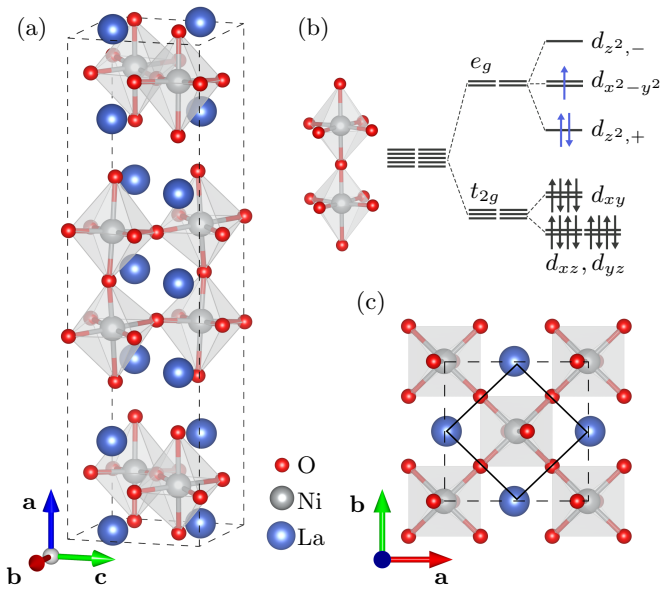


FIG. 1. **Crystal structure and low-energy configuration of bilayer $\text{La}_3\text{Ni}_2\text{O}_7$.** (a) Conventional unit cell ($Z = 4$) of the $Cmcm$ phase, characterized by tilted NiO_6 octahedra, shown in gray. (b) Crystal field splitting and orbital-selective e_g configuration (blue) of two $\text{Ni}^{2.5+}$ cations in a dimer. The d_{z^2} orbitals form bonding $d_{z^2,+}$ and anti-bonding $d_{z^2,-}$ states. (c) Top view of a NiO_2 bilayer with tilted NiO_6 octahedra. Solid and dashed black frames represent the $Fm\bar{3}m$ and $Cmcm$ unit cells, respectively.

XRD experiments identified the high-pressure phase at a much lower temperature of ~ 40 K to be a third, tetragonal ($a = b$), phase with space group $I4/mmm$ [53], in agreement with DFT predictions at 0 K [54]. However, the precise locations of the boundaries between the different structural phases in the complete pressure-temperature (PT) phase diagram remain to be determined.

In this work, we conduct first-principles calculations to correlate the experimentally observed right-triangular superconducting region in the PT-phase diagram of bilayer $\text{La}_3\text{Ni}_2\text{O}_7$ with structural variations and, importantly, their screening effect on the strongly correlated e_g states. We first perform enthalpic optimization to study the structural phase stability at zero temperature under varying hydrostatic pressure. As in previous DFT studies we find that increasing the pressure not only leads to a metallization of the d_{z^2} bands, but also brings the La $5d$ bands substantially closer to the Fermi energy. This energetic effect, together with changes in the spatial overlap between different maximally localized Wannier states triggered by the structural transition, makes that the interaction between electrons in the d_{z^2} and $d_{x^2-y^2}$ bands, and in particular its screening by the La bands, is highly sensitive to pressure. To arrive at a quantitative statement we derive the effective interactions for the electronic states in the dimer configuration in Fig. 1(b) by down-folding the optimized electronic structure to an effective

bilayer model. Via this procedure we find that the Hubbard U parameters of the bilayer model are enhanced by $\sim 30\%$ in the pressure range where superconductivity is observed. The hopping parameters, including the inter-layer hopping, vary significantly less with pressure. We believe that our results provide a starting point for future studies exploring the pairing mechanism in bilayer $\text{La}_3\text{Ni}_2\text{O}_7$ via low-energy models constructed from first principles.

To further confirm the crucial role of the rare-earth d bands we have performed finite-temperature *ab initio* molecular dynamics (AIMD) simulations on $\text{La}_3\text{Ni}_2\text{O}_7$, and zero-temperature DFT simulations on $\text{Ac}_3\text{Ni}_2\text{O}_7$. The AIMD simulations allow us to explicitly verify the effects of the pressure-enhanced spatial proximity of La atoms to the NiO_6 octahedra, which leads to a substantial increase in screening in the parameter range where we find a decrease in the Hubbard U parameters. As a by-product, our AIMD simulations also show that the right-triangle superconducting region is contained entirely in the $I4/mmm$ region of the PT-phase diagram, making it unlikely that the temperature-driven structural transition at high pressure is important for superconductivity. Finally, we investigate the effect of replacing La with Ac, which leads to a higher chemical pressure. Up to an overall rescaling, the parameters of the bilayer model obtained for $\text{Ac}_3\text{Ni}_2\text{O}_7$ at 4 GPa are almost identical to the bilayer model for $\text{La}_3\text{Ni}_2\text{O}_7$ at 20 GPa, and thus both models have roughly the same U/t ratio. This again confirms the crucial role of the rare-earth element in determining the effective interaction strength between electrons in the d_{z^2} and $d_{x^2-y^2}$ transition-metal bands.

II. METHODS

The first-principles DFT calculations are performed using the Vienna Ab initio Simulation Package (VASP) employing the Perdew-Burke-Ernzerhof (PBE) exchange-correlation functional and the projector-augmented-wave formalism with a plane-wave energy cut-off of 600 eV [55–58]. Gaussian smearing with a width of 0.04 eV is used for the Fermi surface broadening. All calculations are performed in the non-magnetic (spin-unpolarized) case. The convergence criterion for the electronic self-consistent loops is set to 10^{-8} eV. Brillouin-zone sampling is Γ -centered where density depends on the considered unit cell, with convergence systematically validated.

Structural optimizations are performed at fixed hydrostatic pressures by minimizing the enthalpy using the conjugate gradient algorithm with respect to all ionic degrees of freedom until the change in total energy subceeds 10^{-7} eV and all Hellmann-Feynman forces subceed 10 meV/Å. Pairwise van der Waals dispersion corrections are included using the DFT-D3 method with Becke-Johnson damping [59]. To avoid finite size effects, the charge densities are calculated on a $5 \times 5 \times 1$ k -point grid in the largest conventional cell of all experimentally known

phases. Initial cells contain distorted Wyckoff positions from experimental data [16].

The AIMD simulations are conducted on a $3 \times 3 \times 1$ k -point grid for the conventional unit cell (Fig. 1(a)) in the isothermal-isobaric (NPT) ensemble, using the Nosé-Hoover thermostat and the Parrinello-Rahman barostat [60–64]. A barostat mass of 2000 amu was employed to maintain stable pressure control. Langevin damping coefficients of 10 ps^{-1} , 5 ps^{-1} , and 2 ps^{-1} were applied to the La, Ni, and O atoms, respectively, while a lattice damping coefficient of 10 ps^{-1} was used. A time step of 1 fs was adopted, with initial configurations equilibrated for 2 ps prior to data collection.

The single-point electronic structures are recalculated on a Γ -centered $5 \times 5 \times 9$ and $9 \times 9 \times 9$ k -point grid for the primitive unit cells in the $Cmcm$ and $I4/mmm$ phase, respectively. The resulting Kohn-Sham bands are downfolded to the e_g dimer configuration using the multi-scale *ab initio* scheme for correlated electrons by Imada *et al.* [65, 66]. This scheme includes the (projector) constrained random phase approximation (cRPA) and tight-binding methodology to obtain the screened Coulomb interactions and hopping integrals, respectively [65, 67]. Static interactions were assumed, as frequency dependence from retarded screening was found to be negligible (see Supplementary Information). To construct a sufficiently localized basis spanning this low-energy subspace, maximally localized Wannier functions (MLWFs) are constructed from projecting the Kohn-Sham orbitals on the e_g orbitals as implemented in Wannier90 [68–70]. The dispersion of the Wannier-interpolated bands is systematically compared to the DFT calculations, confirming a faithful disentanglement. Further details on the Wannierization and downfolding methodology can be found in Section S2 of the Supplementary Information. All implemented VASP input files and post-processing scripts are available from the online GitHub repository or upon request from the authors.

III. RESULTS

A. Structural Optimization

Fig. 2(a) shows the optimized lattice constants of the conventional unit cell of $\text{La}_3\text{Ni}_2\text{O}_7$, shown in Fig. 1(a), at hydrostatic pressures ranging from 0 to 100 GPa. As discussed in Section S1 of the Supplementary Information, we focus on the bilayer structure, as the experimentally observed alternating monolayer-trilayer polymorphic structure exhibits higher enthalpy within the considered pressure range. Two distinct regimes in both degeneracy and slopes can be observed. In the low-pressure region up to *sim*12 GPa, the in-plane lattice constants a and b as shown in Fig. 1(c), are non-degenerate. At higher external pressures, however, they become equal, thereby eliminating the Jahn-Teller distortion in the ab -plane. This explicitly confirms the absence of a zero-

temperature, high-pressure orthorhombic ($a \neq b$) $Fmmm$ phase.

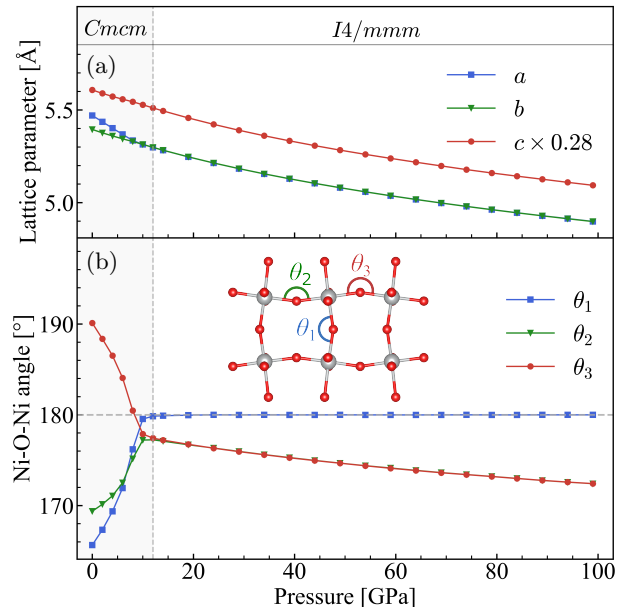


FIG. 2. **Enthalpic optimization of bilayer $\text{La}_3\text{Ni}_2\text{O}_7$.** (a) Lattice constants of the conventional unit cell at hydrostatic pressures between 0 and 100 GPa. The Jahn-Teller distortion in the ab -plane is removed at pressures above 10 GPa. (b) The three inequivalent Ni-O-Ni bond angles of the $Cmcm$ phase. The two basal angles θ_2 and θ_3 in the $Cmcm$ phase (gray) become equal in the $I4/mmm$ phase (above 12 GPa), and coincidentally the NiO_6 octahedra align along the c -axis ($\theta_1 = 180^\circ$).

Fig. 2(b) shows the three inequivalent Ni-O-Ni bond angles in the $Cmcm$ phase. The interlayer bond angle θ_1 straightens completely (*i.e.* becomes equal to 180°) at the transition to the tetragonal phase around 12 GPa, indicating the alignment of the NiO_6 octahedra along the c -axis. Furthermore, the two inequivalent basal bond angles in the low-pressure structures, θ_2 and θ_3 , become equal and both face inwards (*i.e.* into the bilayer), which restores periodicity in the ab -plane, as depicted in Fig. 1(c). The combined result of the symmetry restoration in the ab -plane and the alignment of the NiO_6 octahedra reproduces the zero-temperature structural transition from the low-pressure phase with space group $Cmcm$ to the high-pressure tetragonal phase with subgroup $I4/mmm$ around 12 GPa. This is also confirmed energetically in Section S1 of the Supplementary Information and is found in previous works [18, 53, 54]. The discrepancy in transition pressure between the first-principles results and experiment may arise from limitations in the PBE-D3 approximation.

In the high-pressure limit the cell contracts isotropically, as can be seen from the parallel curves corresponding to the three lattice constants in Fig. 2(a). How-

ever, the crystal structure in the $I4/mmm$ phase compresses anisotropically as the in-plane angle θ_2 in Fig. 2(b) reaches its maximum value of $\sim 177.4^\circ$ near the structural transition and then decreases monotonically within the $I4/mmm$ phase with increasing pressure. This buckling effect can be explained by the La ions from the neighboring rock-salt layers, closing in on the bilayers along the c -axis as the pressure increases. In the next section we will examine the impact of the structural phase transition and the high-pressure compression on the (low-energy) electronic structure.

B. Electronic Structure and Dimer Model

Fig. 3(a) presents the lm -decomposed band structure at 40 GPa, referenced to the Fermi energy (E_F) and projected onto the Ni e_g orbitals. The projection onto the La $d_{x^2-y^2}$ is superimposed as purple circles, with radii representing the absolute overlap value. The four bands closest to the Fermi energy clearly exhibit e_g character, with the individual contributions from d_{z^2} and $d_{x^2-y^2}$ varying significantly across the Brillouin zone. Importantly, the negligible contribution from other spherical harmonics allows us to disentangle the four e_g bands from the higher-energy bands by using the projection method devised for the Wannierization of non-isolated bands [70]. The resulting Wannier interpolation in Fig. 3(a) validates this disentanglement procedure, and confirms that the MLWFs define a suitable subspace for capturing the orbital-selective behavior of two $\text{Ni}^{2.5+}$ cations in adjacent layers.

For the $I4/mmm$ phase, the evolution of the DFT band structure with pressure is shown in Fig. 3(b). We see that most (high-energy) bands tend to move away from E_F under increasing pressure, and the e_g bands become more dispersive. Remarkably, near the Γ -point, we also see that at high hydrostatic compression the La $5d_{x^2-y^2}$ conduction band moves below the e_g bands and eventually below the Fermi energy as well, forming an additional electron pocket. As we will show below, this lowering of the La band has a significant effect on the effective low-energy physics.

To understand the origin of superconductivity in bilayer $\text{La}_3\text{Ni}_2\text{O}_7$, it is crucial to develop an effective model that adequately describes the low-energy electrons near the Fermi surface. Here we use the multi-scale *ab initio* scheme for correlated electrons to construct an effective model for the e_g bands that approximately incorporates the influence of high-energy electrons and holes, and in particular their effect on screening, via many-body perturbation theory [65, 66]. The outcome of this procedure is a generalized Hubbard model, *i.e.* a tight-binding model supplemented with short-range interactions, defined on a bilayer square lattice with two orbitals on each site (see Fig. 3(d)). The generalized Hubbard model for the e_g bands of $\text{La}_3\text{Ni}_2\text{O}_7$ is also often called the *dimer model*. By downfolding the electronic structure of each optimized

crystal structure onto the corresponding MLWFs, Fig. 3(c) shows the pressure dependence of the largest hopping integrals and screened Coulomb interactions, which constitute the parameters of the Hubbard model.

We see that the on-site repulsion energies, $U_{x^2-y^2}$, U_{z^2} and U_{12} in Fig. 3(c), are significantly enhanced in the pressure range 10–60 GPa (even up to $\sim 30\%$), which almost exactly coincides with the range where the strongest superconductivity develops [16, 17]. The change in the hopping integrals, on the other hand, is monotonous and smaller (on the order of 20% at the largest pressures). The sudden increase above 80 GPa is due to the crossing of the La bands below the Fermi energy, which alters the virtual excitations in the cRPA polarization. This signals a breakdown of the four-orbital dimer model (at these pressures one should start to include the La states in the low-energy model), as indicated by the red shaded region above 80 GPa in Fig. 3(c). Nevertheless, for hydrostatic pressures between 0 and 80 GPa, the cRPA screening provides a quantitative insight into the effects of compression. The decreasing U/t trend in both the $Cmcm$ phase and the extreme pressure limit clearly weakens electronic correlations. Technical details of the used algorithms, additional lm -decomposed band structures and corresponding Wannier interpolated bands (with disentanglement windows and MLWF spreads) are given in the Supplementary Information.

We can understand the pressure-dependence of the dimer or Hubbard model parameters as follows. In the low-pressure limit, the $Cmcm$ phase hosts a checkerboard pattern with two distinct tilted NiO_6 octahedra (see Fig. 1(c)). Consequently, the nearest-neighbor hopping integrals, especially the interlayer hopping $t_{z^2}^z$, are weakened due to the increased bond angles which reduce orbital overlap. The reduced symmetry also separates the in-plane hopping into two components: one corresponding to the inward-facing ($t_{x^2-y^2}^x$) and one for the outward-facing ($t_{x^2-y^2}^y$) angles. However, the difference between these parameters is minimal, remaining below 1%, which allows us to treat them as equivalent and maintain a minimal unit cell for the dimer model. The decrease in interaction parameters U_i in the $Cmcm$ phase can be understood from the enhanced screening by the La $5d_{x^2-y^2}$ orbitals, which overlap more strongly with the neighboring e_g -like MLWFs due to the tilted octahedral configuration. However, the decrease in U_i cannot be entirely attributed to screening, as we find that the bare (*i.e.* unscreened) interactions V_i also decrease in the $Cmcm$ phase (see Fig. 3(c)). This can be explained by the same octahedral tilts, which lead to a reduced atomic orbital character and associated delocalization (increased spreads) of the MLWFs in the $Cmcm$ phase (see Supplementary Information).

In the high-pressure limit, Fig. 2 shows a clear compression of the crystal structure in the $I4/mmm$ phase. This results in an enhanced overlap between nearby MLWFs, which monotonically increases the hopping integrals. The compression also decreases the MLWF spreads, which leads to increasing values of Δ (the en-

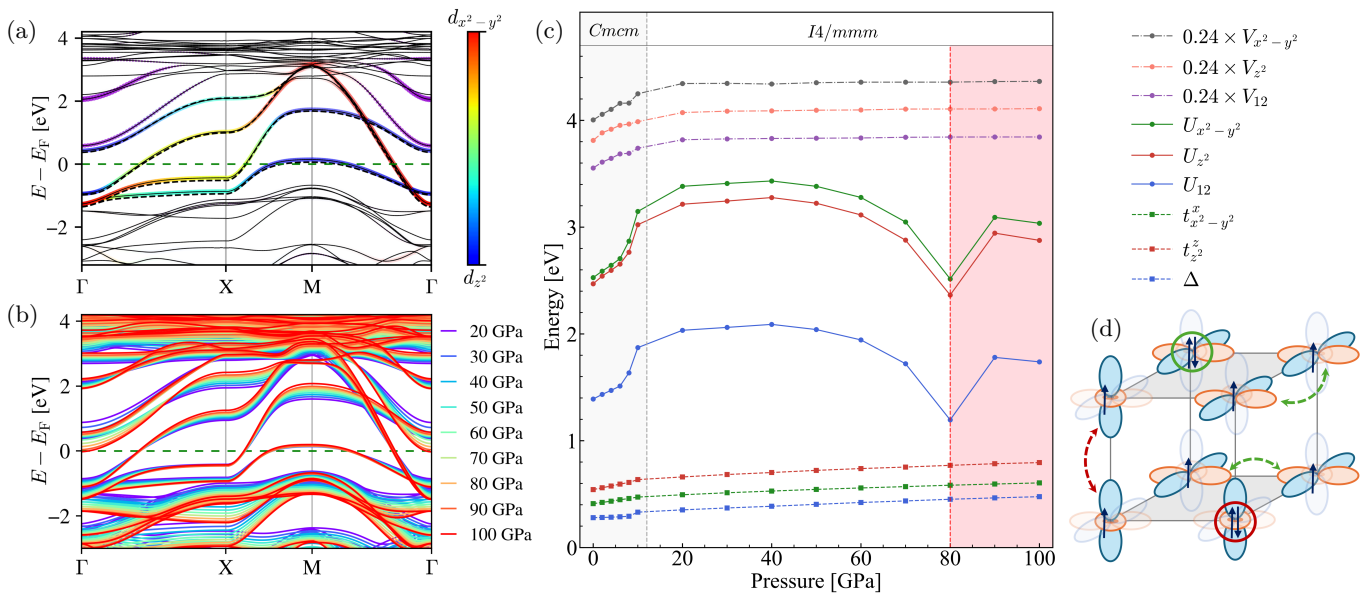


FIG. 3. **Pressure dependence of the band structure and dimer model of bilayer $\text{La}_3\text{Ni}_2\text{O}_7$.** (a) Band structure at 40 GPa, shown as solid black lines, with the superimposed color scale indicating the relative lm -projected weight of the different Ni e_g orbitals. The projection onto the La $d_{x^2-y^2}$ is superimposed as purple circles, with radii representing the corresponding weight. The Wannier-interpolated bands obtained from the four MLWFs are shown as dashed lines. (b) DFT band structures at pressures between 20 GPa and 100 GPa. (c) Pressure dependence of the largest parameters in the low-energy dimer or Hubbard model for the e_g bands of $\text{La}_3\text{Ni}_2\text{O}_7$, as shown in (d). The on-site interaction parameters $U_{x^2-y^2}$, U_{z^2} ($V_{x^2-y^2}$, V_{z^2}) represent the screened (bare) Coulomb interaction for two electrons occupying the MLWF with $d_{x^2-y^2}$ and d_{z^2} character, respectively. The screened (bare) direct interaction between electrons occupying the two different on-site MLWF is given by U_{12} (V_{12}). $\Delta = \epsilon(d_{x^2-y^2}) - \epsilon(d_{z^2})$ is the energy difference between the orbitals, and the tight-binding parameters $t_{x^2-y^2}^x$ and $t_{z^2}^z$ respectively represent nearest-neighbor intra-layer hopping between $d_{x^2-y^2}$ orbitals and nearest-neighbor inter-layer hopping between d_{z^2} orbitals. The pink region represents the pressure range for which the dimer model breaks down.

ergy difference between d_{z^2} and $d_{x^2-y^2}$ orbitals) and bare on-site interactions V_i . At the same time, the effect of screening, which is made explicit by comparing the bare and screened interaction parameters in Fig. 3(c), becomes particularly important at high pressures. We see that screening counteracts the effects of increased localization, and becomes dominant around 40 GPa, after which the effective interaction parameters start to decrease until ~ 80 GPa, where the four-band Ni dimer model breaks down. We attribute the enhanced screening at high pressures to the La $5d$ conduction bands, which lower in energy near the Γ -point, where they have $d_{x^2-y^2}$ character, and which spatially enclose the e_g MLWFs.

C. Molecular Dynamics

Next we include finite temperature (10–100 K) effects through AIMD simulations, extending pressure-driven structural and electronic trends along the temperature axis. For technical details about the AIMD simulations we refer to Section S3 of the Supplementary Information. The top panel in Fig. 4(a) shows the time-averaged (*i.e.* averaged over the simulated trajectory) absolute value of the difference between the in-plane lattice constants a and b . This is a measure for the finite-temperature fluc-

tuations in $a - b$ away from zero. We see that $\langle |a - b| \rangle$ is order ~ 0.1 Å at low temperatures and low pressures corresponding to the orthorhombic $Cmcm$ phase. Upon increasing pressure $\langle |a - b| \rangle$ quickly drops to ~ 0.01 Å in the tetragonal $I4/mmm$ phase. The region of rapid decrease in $\langle |a - b| \rangle$ extends almost perfectly vertically in the PT-phase diagram (*i.e.* parallel to temperature axis), up to the maximum temperature of 100 K used in this work. This suggests that also the $Cmcm - I4/mmm$ phase boundary is approximately independent of temperature up to at least 100 K. This can be confirmed by looking at $a - b$ histograms, as shown in the bottom panel of Fig. 4(a). In the region of large $\langle |a - b| \rangle$, we see that the $a - b$ histograms are centered around $a - b \approx 0.1$ Å, both at $T = 10$ K and $T = 50$ K. In the region of small $\langle |a - b| \rangle$, on the other hand, the $a - b$ histograms are clearly centered around 0 at both $T = 10$ K and $T = 50$ K. This implies that the temperature-driven transition from the high-pressure $I4/mmm$ tetragonal phase found in DFT to the orthorhombic $Fmmm$ phase observed in XRD at room temperature must occur at temperatures above 100 K, placing this structural transition at a comfortable distance from the superconducting region.

The time-averaged interlayer angle θ_1 is shown in the top panel of Fig. 4(b). Note that θ_1 is defined similarly as the polar angle in spherical coordinates, and hence

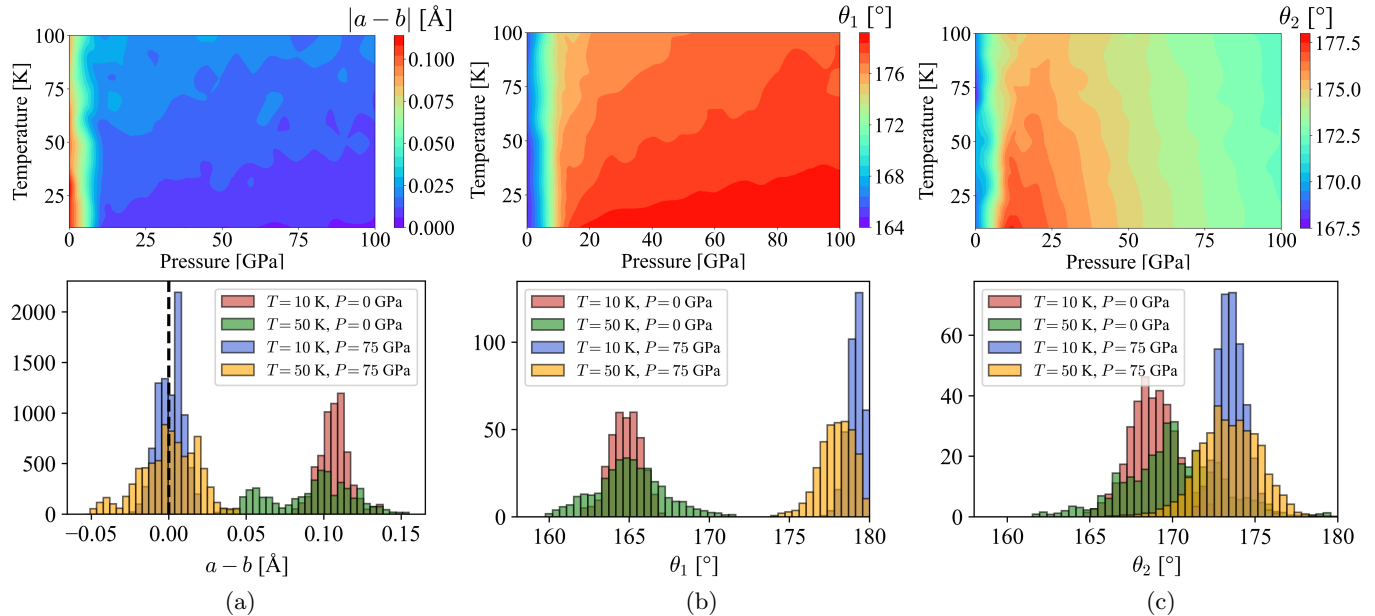


FIG. 4. **AIMD simulations of bilayer $\text{La}_3\text{Ni}_2\text{O}_7$ in the range of 10–100 K and 0–100 GPa.** The upper row shows the time-averages of the full diagram, while the lower row displays frequency histograms at four indicated pressure-temperature points. (a) Difference between lattice constants, a and b , of the conventional unit cell, showing absolute differences due to oscillations between a and b lattice constants. (b) Interpolated colormap of the interlayer angle θ_1 . (c) Interpolated colormap of the inwards basal angle θ_2 .

lies in the range $[0, 180^\circ]$, with $\theta_1 = 180^\circ$ representing a fully straightened bond. With this definition, we will use $\langle \theta_1 \rangle$ as a measure for the fluctuations away from $\theta_1 = 180^\circ$. The reduced bin size near $\theta_1 = 180^\circ$ reflects the unscaled space angle, resulting from azimuthal freedom. We see from Fig. 4(b) that $\langle \theta_1 \rangle$ exhibits two distinct trends. First, approximately independent of temperature, $\langle \theta_1 \rangle$ quickly increases from $\sim 165^\circ$ to $\sim 180^\circ$ around a pressure of 10 GPa. This we attribute to the octahedral tilt which disappears upon going from $Cmcm$ to $I4/mmm$, which can be verified explicitly from the histograms in the lower panel of Fig. 4(b): the low-pressure histograms are centered around $\sim 165^\circ$ while the high-pressure histograms are centered around $\sim 180^\circ$. The verticality of the region where $\langle \theta_1 \rangle$ quickly rises agrees with orthorhombic-tetragonal transition discussed above – both pointing to an approximately temperature-independent $Cmcm - I4/mmm$ phase boundary below 100 K. This result indicates that the experimentally observed superconducting region is contained entirely within the $I4/mmm$ phase. Secondly, inside the $I4/mmm$ phase, increasing the temperature reduces $\langle \theta_1 \rangle$ due to enhanced thermal fluctuations. At pressures right after the structural transition (14–20 GPa), we see that increasing the temperature significantly affects the interlayer angle. Higher hydrostatic pressure, in turn, enhances the robustness of octahedral alignment against thermal fluctuations, which was validated by equivalent frequency histograms in Section S3 of the Supplementary Information.

Also $\langle \theta_2 \rangle$, the average of the basal Ni-O-Ni bond angle

$\theta_2 \in [0, 180^\circ]$, exhibits a narrow region of rapid increase at the $Cmcm - I4/mmm$ phase boundary, as shown in the top panel of Fig. 4(c). At higher pressures, we see that crystal compression leads to a decreasing value of $\langle \theta_2 \rangle$, due to the La ions approaching the NiO layers along the c -axis as observed at 0 K in Fig. 2(b). Increasing temperature also reduces $\langle \theta_2 \rangle$. From the histograms in the bottom panel of Fig. 4(c) we see that θ_2 is sufficiently far away from 180° to be able to conclude that the decrease in $\langle \theta_2 \rangle$ is not a fluctuation effect, but indicates a true shift in average value of the basal bond angle.

The AIMD results, together with the discussion in Subsection III B, suggest following picture underlying the experimentally observed right-triangle-shaped superconducting region in the PT-phase diagram [18]. First, the rapid increase of the superconducting transition temperature T_c at the critical pressure can be related to the almost vertical $Cmcm - I4/mmm$ phase boundary where the octahedral tilt disappears. Secondly, for pressures larger than ~ 18 GPa, T_c is observed to start decreasing, which coincides with the region of decreasing θ_2 . Recall that latter can be taken as a proxy for the spatial overlap between the La states and the MLWFs of the e_g bands: smaller θ_2 means larger overlap and hence more screening. Besides thermal fluctuations of the superconducting condensate itself, another detrimental finite-temperature effect for superconductivity could therefore be that the basal angle decreases upon raising the temperature, giving rise to increased screening at higher temperature. This effect could contribute to the decrease of T_c with pressure.

D. Chemical Substitution

Our analysis of bilayer $\text{La}_3\text{Ni}_2\text{O}_7$ can now be used as a guiding principle for the design of bulk nickelates superconducting near ambient conditions. The most straightforward adaptation is an isoelectronic substitution of the rare-earth A -site cation La^{3+} , which plays a pivotal role in the structural phase transition and corresponding critical pressure. Doping with smaller atoms was initially expected to stabilize the tetragonal phase at ambient conditions via chemical precompression. However, DFT simulations on $\text{A}_3\text{Ni}_2\text{O}_7$ showed the opposite: smaller atoms increased the transition pressure from the orthorhombic to the tetragonal structure [54]. Consequently, larger substituents were proposed to stabilize the $I4/mmm$ structure by the inherent chemical pressure, replacing external hydrostatic pressure. Among (valence) isoelectronic elements, only Ac^{3+} possesses a larger ionic radius, for which $\text{Ac}_3\text{Ni}_2\text{O}_7$ was indeed found to be structurally stable in the $I4/mmm$ phase at ambient pressure, as confirmed by DFT+ U calculations [71, 72].

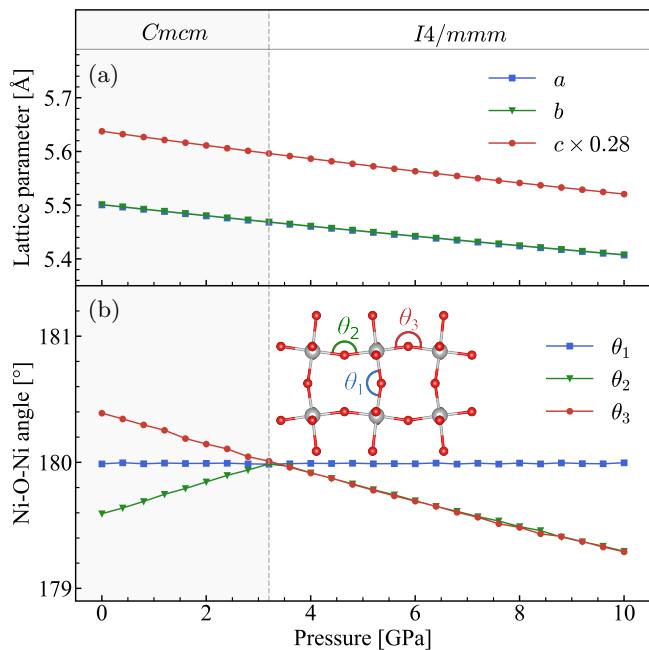


FIG. 5. **Enthalpic optimization of bilayer $\text{Ac}_3\text{Ni}_2\text{O}_7$.** (a) Lattice constants of the conventional unit cell (as shown for $\text{La}_3\text{Ni}_2\text{O}_7$ in Fig. 1(a)) at hydrostatic pressures between 0 and 10 GPa. (b) The three unique Ni-O-Ni bond angles of the $Cmcm$ phase.

Enthalpic optimization of bilayer $\text{Ac}_3\text{Ni}_2\text{O}_7$ at external pressures between 0 and 10 GPa, as shown in Fig. 5, confirms the absence of Jahn-Teller distortion in the ab -plane, which is likely due to the increased chemical pressure of the larger Ac^{3+} cations. However, we find that the in-plane spatial symmetry is still (slightly) broken at pressures up to 3.2 GPa. The two inequivalent basal angles θ_2 and θ_3 become equal with NiO_6 octahe-

TABLE I. **Dimer models for $\text{La}_3\text{Ni}_2\text{O}_7$ and $\text{Ac}_3\text{Ni}_2\text{O}_7$** Comparison of the dimer models for bilayer $\text{La}_3\text{Ni}_2\text{O}_7$ at 20 GPa and bilayer $\text{Ac}_3\text{Ni}_2\text{O}_7$ at 4 GPa.

Parameter [eV]	$\text{La}_3\text{Ni}_2\text{O}_7$	$\text{Ac}_3\text{Ni}_2\text{O}_7$
$U_{x^2-y^2}$	3.3826	3.0284
U_{z^2}	3.2149	2.9291
V	2.0342	1.7342
$t_{x^2-y^2}^x$	0.4939	0.4268
$t_{z^2}^z$	0.6609	0.5797
Δ	0.3526	0.2930

dral alignment in the $I4/mmm$ phase above 3.2 GPa. The presence of a low-pressure $Cmcm$ phase could arise from limitations in the PBE-D3 level, as opposed to the DFT+ U methodology used in Ref. [71], which takes more electronic correlations into account and found an $I4/mmm$ phase already at 0 GPa. Nonetheless, the significantly lower critical pressure found in this work, resulting from the enlarged ionic radius, confirms the important role of chemical pressure exerted by the A -site cations. The basal angle in the $I4/mmm$ phase furthermore decreases faster than in $\text{La}_3\text{Ni}_2\text{O}_7$, which can also be ascribed to the enhanced chemical pressure of the larger Ac^{3+} cations.

Apart from its crucial role in pressure-driven structural deformation, we have argued above that the La $5d$ bands are also important in providing significant screening effects, which we suggest reduce the superconducting T_c at higher external pressures. The band structures of $\text{La}_3\text{Ni}_2\text{O}_7$ and $\text{Ac}_3\text{Ni}_2\text{O}_7$ are known to be nearly identical (as confirmed in the Supplementary Information) [71]. The low-energy parameters of the dimer model are compared for $\text{La}_3\text{Ni}_2\text{O}_7$ at 20 GPa and $\text{Ac}_3\text{Ni}_2\text{O}_7$ at 4 GPa in Table I. The on-site screened Coulomb interactions in 4 GPa $\text{Ac}_3\text{Ni}_2\text{O}_7$ are clearly smaller in value than in ideally pressurized $\text{La}_3\text{Ni}_2\text{O}_7$, which can be explained by the larger lattice constants and consequent decreased localization of the MLWFs. However, the hopping integrals are also smaller, which can be explained by the reduced MLWF overlap as a result of the larger Ni-Ni distances. Thus, up to an overall rescaling, the dimer models shown in Table I are very similar. This indeed hints at the possibility of ambient pressure superconductivity in $\text{Ac}_3\text{Ni}_2\text{O}_7$, and confirms the important role of the rare-earth element in determining the screened interaction parameters for the electrons in the e_g bands. Even though $\text{Ac}_3\text{Ni}_2\text{O}_7$ is not a viable option for practical use because of actinium's intense radioactivity, our results nevertheless confirm the essential role of the A -site cations as discussed throughout this work.

IV. CONCLUSIONS

We performed first-principles calculations on pressurized $\text{La}_3\text{Ni}_2\text{O}_7$, using the results to develop low-energy models for the electronic structure near the Fermi energy. This was achieved by downfolding the DFT band structures to maximally localized Wannier functions (MLWFs), which capture the orbital-selective $(2\text{Ni})^{5+}$ configuration. The resulting screened interaction terms and hopping integrals allow us to correlate pressure-driven structural trends to the stability of the experimentally observed superconducting phase. Our DFT optimizations confirmed a previously-found structural phase transition from the orthorhombic $Cmcm$ phase to the tetragonal $I4/mmm$ phase at approximately 12 GPa. At this structural transition, which roughly coincides with the onset of superconductivity in experiment, we found a significant increase in the on-site repulsion for electrons in the MLWFs spanning the e_g bands. At higher pressures, we found a decreasing trend in the effective interactions. We attributed both these trends to the important role of the La $5d$ conduction bands, and in particular their role in screening the interactions between the e_g electrons. An intuitive understanding of this screening effect can be obtained from simple geometric considerations, such as the alignment of the NiO_6 octahedra at low pressure, and increased buckling causing smaller basal Ni-O-Ni bond angles at higher pressures.

Ab initio molecular dynamics simulations further extended our results to finite temperatures, providing a more complete understanding of the experimentally observed pressure-temperature phase diagram, and in particular the embedding of the superconducting region inside the structural $I4/mmm$ phase. For one, the inter-layer alignment of the octahedra, which proved to be essential in the stabilization of the superconducting phase, becomes robust against thermal oscillations with increased pressure. Another important effect is that the basal Ni-O-Ni angle folding increases both with pressure and temperature. The enhanced screening from the enclosing La ions at higher temperature can thus help destabilize the superconducting phase. The combination of the observed structural trends and their effect on the dimer model parameters for the low-energy e_g electrons provide important clues to explain the experimentally observed right-triangle shape of the superconducting region in the temperature-pressure phase diagram. Finally, we also replaced La with the larger isoelectronic element Ac in our DFT simulations. Up to an overall smaller energy

scale caused by a larger lattice constant, the low-energy dimer model obtained for $\text{Ac}_3\text{Ni}_2\text{O}_7$ at 4 GPa is remarkably similar to that of $\text{La}_3\text{Ni}_2\text{O}_7$ at 20 GPa, which confirms that the most important changes experienced by the e_g electrons under increasing pressure are indeed determined by the rare-earth elements.

ACKNOWLEDGMENTS

This work is supported by the Research Board of Ghent University (BOF) through a Concerted Research Action (BOF23/GOA/021). V. V. S. acknowledges the Research Board of Ghent University (BOF). The computational resources (Stevin Supercomputer Infrastructure) and services used in this work were provided by VSC (Flemish Supercomputer Center), funded by Ghent University, FWO, and the Flemish Government—department EWI. N. B. was supported by the European Research Council under the European Union Horizon 2020 Research and Innovation Programme via Grant Agreement No. 101076597-SIESS, and by a grant from the Simons Foundation (SFI-MPS-NFS-00006741-04).

SUPPORTING INFORMATION AVAILABLE

Computational data supporting the results of this work are available from the online GitHub repository at <https://github.com/daanverraes/Supporting-Information> or upon request from the authors. A more elaborate discussion of the results can be found in the Supplementary Information.

AUTHOR CONTRIBUTIONS

D. V., T. B., N. B. and V. V. S. initiated the discussion, designed the paper, and were involved in the discussion of the results. D. V. and N. B. wrote the manuscript with contributions of all authors. D. V. performed all simulations.

COMPETING INTERESTS

The authors declare no competing interests.

-
- [1] J. G. Bednorz and K. A. Müller, *Z. Physik B - Condensed Matter* **64**, 189 (1986).
 [2] P. W. Anderson, *Science* **235**, 1196 (1987).
 [3] B. Keimer, S. A. Kivelson, M. R. Norman, S. Uchida, and J. Zaanen, *Nature* **518**, 179 (2015).

- [4] M. A. Hayward, M. A. Green, M. J. Rosseinsky, and J. Sloan, *J. Am. Chem. Soc.* **121**, 8843 (1999).
 [5] A. V. Boris, Y. Matiks, E. Benckiser, A. Frano, P. Popovich, V. Hinkov, P. Wochner, M. Castro-Colin, E. Detemple, V. K. Malik, C. Bernhard, T. Prokscha, A. Suter, Z. Salman, E. Morenzoni, G. Cristiani, H.-U.

- Habermeier, and B. Keimer, *Science* **332**, 937 (2011).
- [6] A. S. Disa, D. P. Kumah, A. Malashevich, H. Chen, D. A. Arena, E. D. Specht, S. Ismail-Beigi, F. Walker, and C. H. Ahn, *Phys. Rev. Lett.* **114**, 026801 (2015).
- [7] V. I. Anisimov, D. Bukhvalov, and T. M. Rice, *Phys. Rev. B* **59**, 7901 (1999).
- [8] V. V. Poltavets, K. A. Lokshin, S. Dikmen, M. Croft, T. Egami, and M. Greenblatt, *J. Am. Chem. Soc.* **128**, 9050 (2006).
- [9] J. Chaloupka and G. Khaliullin, *Phys. Rev. Lett.* **100**, 016404 (2008).
- [10] G. Zhou, F. Jiang, J. Zang, Z. Quan, and X. Xu, *ACS Appl. Mater. Interfaces* **10**, 1463 (2018).
- [11] J. Zhang, A. S. Botana, J. W. Freeland, D. Phelan, H. Zheng, V. Pardo, M. R. Norman, and J. F. Mitchell, *Nature Phys* **13**, 864 (2017).
- [12] D. Li, K. Lee, B. Y. Wang, M. Osada, S. Crossley, H. R. Lee, Y. Cui, Y. Hikita, and H. Y. Hwang, *Nature* **572**, 624 (2019).
- [13] M. Osada, B. Y. Wang, K. Lee, D. Li, and H. Y. Hwang, *Physical Review Materials* **4**, 121801 (2020).
- [14] G. A. Pan, D. Ferenc Segedin, H. LaBollita, Q. Song, E. M. Nica, B. H. Goodge, A. T. Pierce, S. Doyle, S. Novakov, D. Córdova Carrizales, A. T. N'Diaye, P. Shafer, H. Paik, J. T. Heron, J. A. Mason, A. Yacoby, L. F. Kourkoutis, O. Erten, C. M. Brooks, A. S. Botana, and J. A. Mundy, *Nat. Mater.* **21**, 160 (2022).
- [15] N. N. Wang, M. W. Yang, Z. Yang, K. Y. Chen, H. Zhang, Q. H. Zhang, Z. H. Zhu, Y. Uwatoko, L. Gu, X. L. Dong, J. P. Sun, K. J. Jin, and J.-G. Cheng, *Nature Communications* **13**, 4367 (2022).
- [16] H. Sun, M. Huo, X. Hu, J. Li, Z. Liu, Y. Han, L. Tang, Z. Mao, P. Yang, B. Wang, J. Cheng, D.-X. Yao, G.-M. Zhang, and M. Wang, *Nature* **621**, 493 (2023).
- [17] Y. Zhang, D. Su, Y. Huang, Z. Shan, H. Sun, M. Huo, K. Ye, J. Zhang, Z. Yang, Y. Xu, Y. Su, R. Li, M. Smidman, M. Wang, L. Jiao, and H. Yuan, *Nat. Phys.* **20**, 1269 (2024).
- [18] J. Li, P. Ma, H. Zhang, X. Huang, C. Huang, M. Huo, D. Hu, Z. Dong, C. He, J. Liao, X. Chen, T. Xie, H. Sun, and M. Wang, *arXiv 10.48550/arXiv.2404.11369* (2024), *arXiv:arXiv:2404.11369*.
- [19] Y. Zhang, L.-F. Lin, A. Moreo, and E. Dagotto, *arXiv 10.48550/arXiv.2306.03231* (2023), *arXiv:arXiv:2306.03231*.
- [20] Z. Luo, X. Hu, M. Wang, W. Wú, and D.-X. Yao, *arXiv 10.48550/arXiv.2305.15564* (2023), *arXiv:arXiv:2305.15564*.
- [21] Y. Gu, C. Le, Z. Yang, X. Wu, and J. Hu, *arXiv 10.48550/arXiv.2306.07275* (2023), *arXiv:arXiv:2306.07275*.
- [22] Z. Luo, B. Lv, M. Wang, W. Wú, and D.-X. Yao, *npj Quantum Materials* **9**, 1 (2024).
- [23] Q.-G. Yang, D. Wang, and Q.-H. Wang, *Phys. Rev. B* **108**, L140505 (2023).
- [24] F. Lechermann, J. Gondolf, S. Bötzel, and I. M. Eremin, *arXiv 10.48550/arXiv.2306.05121* (2023), *arXiv:arXiv:2306.05121*.
- [25] Y. Shen, M. Qin, and G.-M. Zhang, *Chinese Physics Letters* **40**, 127401 (2023).
- [26] H. Sakakibara, N. Kitamine, M. Ochi, and K. Kuroki, *Phys. Rev. Lett.* **132**, 106002 (2024).
- [27] C. Lu, Z. Pan, F. Yang, and C. Wu, *Phys. Rev. Lett.* **132**, 146002 (2024).
- [28] Z. Liao, L. Chen, G. Duan, Y. Wang, C. Liu, R. Yu, and Q. Si, *Phys. Rev. B* **108**, 214522 (2023).
- [29] X.-Z. Qu, D.-W. Qu, J. Chen, C. Wu, F. Yang, W. Li, and G. Su, *Phys. Rev. Lett.* **132**, 036502 (2024).
- [30] Y.-f. Yang, G.-M. Zhang, and F.-C. Zhang, *Phys. Rev. B* **108**, L201108 (2023).
- [31] W. Wú, Z. Luo, D.-X. Yao, and M. Wang, *Sci. China Phys. Mech. Astron.* **67**, 117402 (2024).
- [32] J. Huang, Z. D. Wang, and T. Zhou, *Phys. Rev. B* **108**, 174501 (2023).
- [33] K. Jiang, Z. Wang, and F.-C. Zhang, *Chinese Phys. Lett.* **41**, 017402 (2024).
- [34] D.-C. Lu, M. Li, Z.-Y. Zeng, W. Hou, J. Wang, F. Yang, and Y.-Z. You, *arXiv 10.48550/arXiv.2308.11195* (2023), *arXiv:arXiv:2308.11195 [cond-mat.supr-con]*.
- [35] H. Oh and Y.-H. Zhang, *Physical Review B* **108**, 174511 (2023).
- [36] Y. Zhang, L.-F. Lin, A. Moreo, T. A. Maier, and E. Dagotto, *Nat Commun* **15**, 2470 (2024).
- [37] T. Kaneko, H. Sakakibara, M. Ochi, and K. Kuroki, *Phys. Rev. B* **109**, 045154 (2024).
- [38] H. Yang, H. Oh, and Y.-H. Zhang, *arXiv e-prints 10.48550/arXiv.2408.01493* (2024), *arXiv:2408.01493*.
- [39] H. Yang, H. Oh, and Y.-H. Zhang, *Phys. Rev. B* **110**, 104517 (2024), *arXiv:2309.15095 [cond-mat.str-el]*.
- [40] D. A. Shilenko and I. V. Leonov, *Phys. Rev. B* **108**, 125105 (2023).
- [41] Y.-H. Tian, Y. Chen, J.-M. Wang, R.-Q. He, and Z.-Y. Lu, *Phys. Rev. B* **109**, 165154 (2024).
- [42] Y.-B. Liu, J.-W. Mei, F. Ye, W.-Q. Chen, and F. Yang, *Phys. Rev. Lett.* **131**, 236002 (2023).
- [43] Y. Cao and Y.-f. Yang, *Phys. Rev. B* **109**, L081105 (2024).
- [44] Q. Qin and Y.-f. Yang, *Phys. Rev. B* **108**, L140504 (2023).
- [45] X. Chen, P. Jiang, J. Li, Z. Zhong, and Y. Lu, *Physical Review B* **111**, 014515 (2025).
- [46] R. Jiang, J. Hou, Z. Fan, Z.-J. Lang, and W. Ku, *Phys. Rev. Lett.* **132**, 126503 (2024).
- [47] V. Christiansson, F. Petocchi, and P. Werner, *Physical Review Letters* **131**, 206501 (2023).
- [48] Y. Zhang, L.-F. Lin, A. Moreo, T. A. Maier, and E. Dagotto, *Phys. Rev. B* **108**, 165141 (2023).
- [49] X.-W. Yi, Y. Meng, J.-W. Li, Z.-W. Liao, J.-Y. You, B. Gu, and G. Su, *Phys. Rev. B* **110**, L140508 (2024).
- [50] J. Chen, F. Yang, and W. Li, *Phys. Rev. B* **110**, L041111 (2024).
- [51] S. N. Ruddlesden and P. Popper, *Acta Cryst* **11**, 54 (1958).
- [52] H. Sakakibara, K. Suzuki, H. Usui, S. Miyao, I. Maruyama, K. Kusakabe, R. Arita, H. Aoki, and K. Kuroki, *Phys. Rev. B* **89**, 224505 (2014).
- [53] L. Wang, Y. Li, S.-Y. Xie, F. Liu, H. Sun, C. Huang, Y. Gao, T. Nakagawa, B. Fu, B. Dong, Z. Cao, R. Yu, S. I. Kawaguchi, H. Kadobayashi, M. Wang, C. Jin, H.-k. Mao, and H. Liu, *J. Am. Chem. Soc.* **146**, 7506 (2024).
- [54] B. Geisler, J. J. Hamlin, G. R. Stewart, R. G. Hennig, and P. J. Hirschfeld, *npj Quantum Mater.* **9**, 1 (2024).
- [55] G. Kresse and J. Hafner, *Phys. Rev. B* **47**, 558 (1993).
- [56] G. Kresse and J. Furthmüller, *Phys. Rev. B* **54**, 11169 (1996).
- [57] J. P. Perdew, K. Burke, and M. Ernzerhof, *Phys. Rev. Lett.* **77**, 3865 (1996).
- [58] P. E. Blöchl, *Phys. Rev. B* **50**, 17953 (1994).

- [59] S. Grimme, J. Antony, S. Ehrlich, and H. Krieg, *The Journal of Chemical Physics* **132**, 154104 (2010).
- [60] S. Nosé, *The Journal of Chemical Physics* **81**, 511 (1984).
- [61] N. Shuichi, *Progress of Theoretical Physics Supplement* **103**, 1 (1991).
- [62] W. G. Hoover, *Phys. Rev. A* **31**, 1695 (1985).
- [63] M. Parrinello and A. Rahman, *Phys. Rev. Lett.* **45**, 1196 (1980).
- [64] M. Parrinello and A. Rahman, *Journal of Applied Physics* **52**, 7182 (1981).
- [65] F. Aryasetiawan, M. Imada, A. Georges, G. Kotliar, S. Biermann, and A. I. Lichtenstein, *Phys. Rev. B* **70**, 195104 (2004).
- [66] M. Imada and T. Miyake, *J. Phys. Soc. Jpn.* **79**, 112001 (2010).
- [67] W. Hanke and L. J. Sham, *Phys. Rev. B* **21**, 4656 (1980).
- [68] N. Marzari and D. Vanderbilt, *Phys. Rev. B* **56**, 12847 (1997).
- [69] G. Pizzi, V. Vitale, R. Arita, S. Blügel, F. Freimuth, G. Géranton, M. Gibertini, D. Gresch, C. Johnson, T. Koretsune, J. Ibañez-Azpiroz, H. Lee, J.-M. Lihm, D. Marchand, A. Marrazzo, Y. Mokrousov, J. I. Mustafa, Y. Nohara, Y. Nomura, L. Paulatto, S. Poncé, T. Ponweiser, J. Qiao, F. Thöle, S. S. Tsirkin, M. Wierzbowska, N. Marzari, D. Vanderbilt, I. Souza, A. A. Mostofi, and J. R. Yates, *J. Phys.: Condens. Matter* **32**, 165902 (2020).
- [70] I. Souza, N. Marzari, and D. Vanderbilt, *Physical Review B* **65**, 035109 (2001).
- [71] L. C. Rhodes and P. Wahl, *Phys. Rev. Materials* **8**, 044801 (2024).
- [72] S. Wu, Z. Yang, X. Ma, J. Dai, M. Shi, H.-Q. Yuan, H.-Q. Lin, and C. Cao, *arXiv 10.48550/arXiv.2403.11713* (2024), *arXiv:arXiv:2403.11713*.
- [73] P. Puphal, P. Reiss, N. Enderlein, Y.-M. Wu, G. Khalullin, V. Sundaramurthy, T. Priessnitz, M. Knauff, A. Suthar, L. Richter, M. Isobe, P. van Aken, H. Takagi, B. Keimer, Y. Suyolcu, B. Wehinger, P. Hansmann, and M. Hepting, *Phys. Rev. Lett.* **133**, 146002 (2024).
- [74] X. Chen, J. Zhang, A. S. Thind, S. Sharma, H. LaBollita, G. Peterson, H. Zheng, D. P. Phelan, A. S. Botana, R. F. Klie, and J. F. Mitchell, *J. Am. Chem. Soc.* **146**, 3640 (2024).
- [75] H. Wang, L. Chen, A. Rutherford, H. Zhou, and W. Xie, *Inorg. Chem.* **63**, 5020 (2024).
- [76] Y. Zhang, L.-F. Lin, A. Moreo, T. A. Maier, and E. Dagotto, *Phys. Rev. B* **110**, L060510 (2024).
- [77] Z. Ouyang, M. Gao, and Z.-Y. Lu, *npj Quantum Mater.* **9**, 1 (2024).
- [78] J. Qiao, J. Zhou, Z. Yuan, and W. Zhao, *Physical Review B* **98**, 214402 (2018).

Supplementary Information:

Evidence for Strongly Correlated Superconductivity in $\text{La}_3\text{Ni}_2\text{O}_7$ from First Principles

Daan Verraes^{1,2}, Tom Braeckvelt¹, and Nick Bultinck², Veronique Van Speybroeck¹

¹*Center for Molecular Modeling, Ghent University, Technologiepark 46, 9052 Zwijnaarde, Belgium*

²*Department of Physics and Astronomy, Ghent University, Krijgslaan 281, 9000 Ghent, Belgium*

(Dated: February 28, 2025)

S1. STRUCTURAL OPTIMIZATION

A. Polymorphic Stability

Experimental studies have reported a biphasic equilibrium between the conventional bilayer polymorph (Fig. S1(a)) and the monolayer-trilayer polymorph (Fig. S1(c)) in samples of $\text{La}_3\text{Ni}_2\text{O}_7$ [73–75]. To fully understand the phase stability in this nickelate from first principles, a comprehensive investigation into the polymorphic stability is essential. Throughout optimization, the initial stacking sequence remains fixed, as both polymorphs are separated by a significant energy barrier, which allows to optimize these separately. The enthalpic difference between the optimized polymorphs is given in Fig. S1(b) at hydrostatic pressures ranging from 0 to 100 GPa. The strictly positive difference suggests that, at low temperatures, bilayer $\text{La}_3\text{Ni}_2\text{O}_7$ is energetically more stable than the monolayer-trilayer polymorph, representing a metastable state for the full pressure range. The difference becomes larger as the pressure increases, extending the findings in refs. [76] and [77]. Accordingly, this work focuses on the enthalpic optimization of the bilayer polymorph.

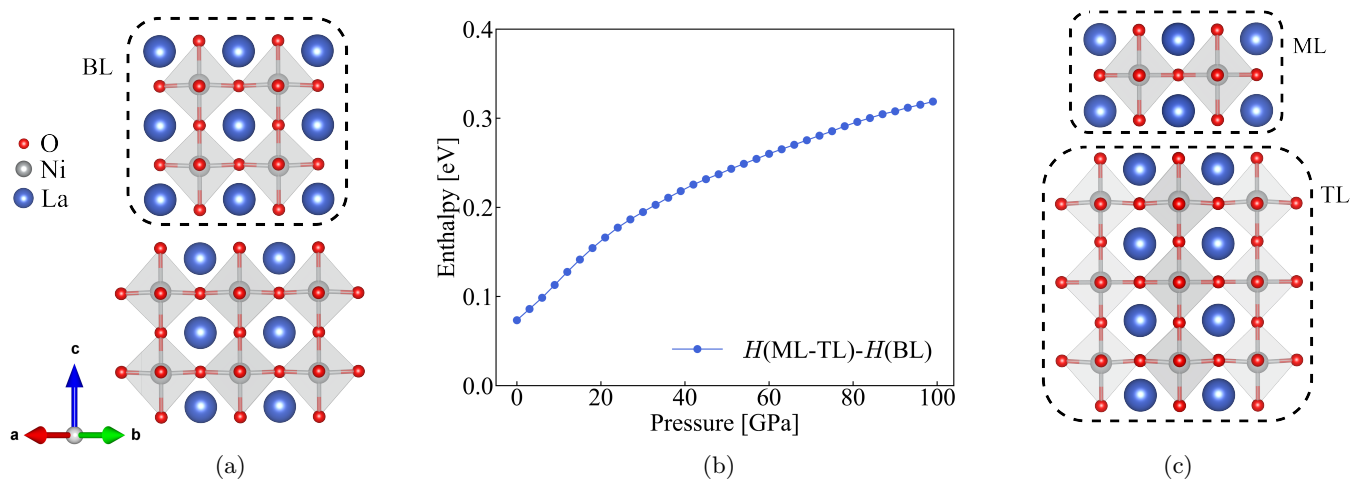


FIG. S1. **Polymorphic stability in $\text{La}_3\text{Ni}_2\text{O}_7$ from first principles.** Perovskite layer stacking in the (a) bilayer (BL) and (c) monolayer-trilayer (ML-TL) polymorph shown in their high-symmetry (tetragonal) phases. (b) The enthalpic difference per structural formula, $H(\text{ML-TL}) - H(\text{BL})$, with respect to the applied hydrostatic pressure ranging from 0 to 100 GPa.

B. Bilayer Phase Stability

The first enthalpic optimizations of bilayer $\text{La}_3\text{Ni}_2\text{O}_7$, shown in Fig. 2 of the main text, are conducted without any restrictions on the conventional unit cell. To ensure that the optimized crystal structure corresponds to an enthalpic minimum, we performed a frequency analysis. The absence of imaginary frequency modes confirms that the structure is at a true minimum. From geometric considerations in Fig. 2, the two discussed structural phases were assigned within specific pressure ranges. This allowed us to improve electronic structures in their primitive unit cells with higher k -point sampling by fixing the spatial symmetries in subsequent optimizations. The initial symmetrized unit cells were made for all pressure points and for both space groups by calculating the corresponding Wyckoff

parameters through averaged atomic distances. The converged enthalpy for the different constrained optimizations were thereafter compared with the original (unbiased) optimized conventional cells and their difference can be seen in Fig. S2. The $Cmcm$ -restricted optimization resulted in enthalpic differences per structural formula with the unbiased optimization of less than 2 meV in the considered pressure range. The notable difference (*i.e.* above 10 meV) with the $I4/mmm$ -restricted optimization up to around 12 GPa confirms the phase transition, discussed in section III B.

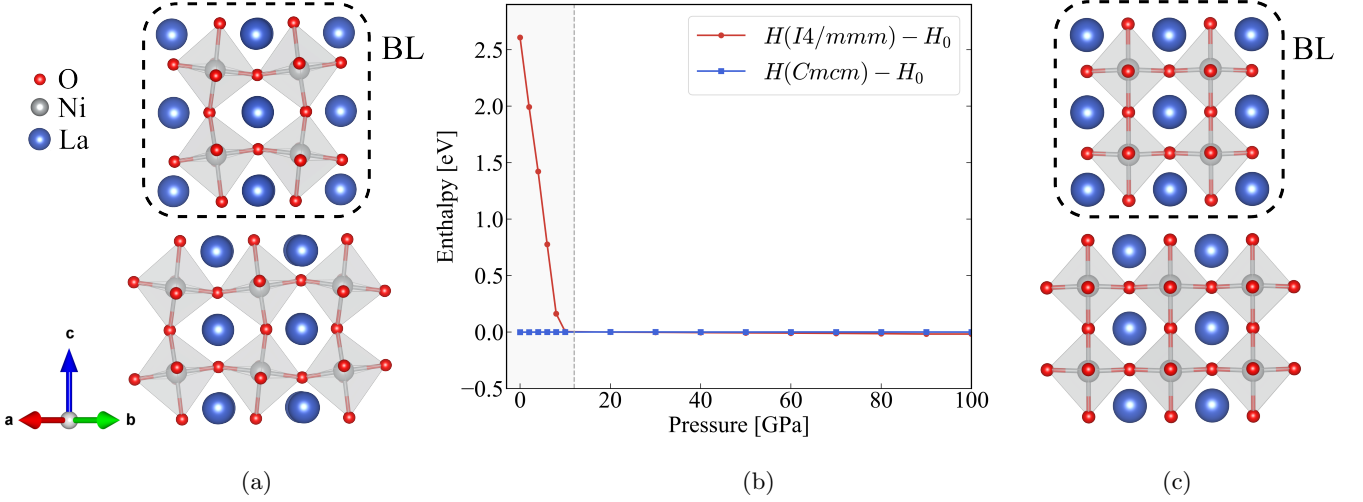


FIG. S2. **Phase stability in bilayer $\text{La}_3\text{Ni}_2\text{O}_7$ from first principles.** (a) Octahedral tilts in the $Cmcm$ phase and (c) alignment in the $I4/mmm$ phase. (b) The enthalpic difference per structural formula between the unrestricted and symmetry-restricted enthalpies, $H(\text{phase}) - H_0$, with respect to the applied hydrostatic pressure ranging from 0 to 100 GPa.

S2. ELECTRONIC STRUCTURE AND DIMER MODEL

A. Band Structure

For several optimized crystal structures, the corresponding electronic structures are calculated in the primitive unit cell. In the low-pressure $Cmcm$ phase, the primitive unit cell contains two times the structural formula, as seen in Fig. S3(a). The single-point electronic structure is calculated on a $5 \times 5 \times 9$ k -mesh. The resulting (pressure-dependent) band structures in Fig. S3(b) show band folding as a consequence of the broken spatial symmetry in the ab -plane.

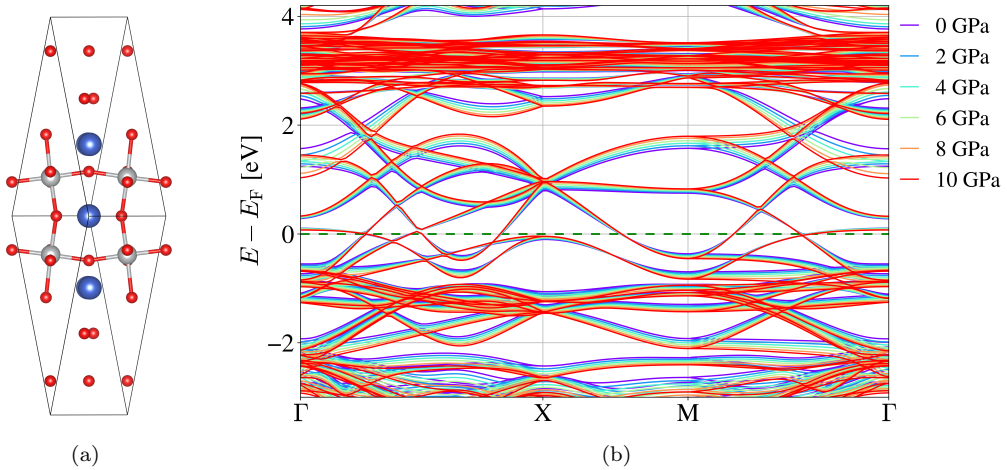


FIG. S3. **Primitive unit cell of bilayer $\text{La}_3\text{Ni}_2\text{O}_7$ in the $Cmcm$ phase and pressure-dependent band structures.** (a) The crystal structure in the primitive unit cell of the $Cmcm$ phase containing one structural formula. The atom types are displayed as represented in Fig. S1. (b) DFT band structures at pressures between 0 GPa and 10 GPa.

In the high-pressure $I4/mmm$ phase, the primitive unit cell contains the structural formula once, as seen in Fig. S4(a). The single-point electronic structure is calculated on a $9 \times 9 \times 9$ mesh. The resulting (pressure-dependent) band structure, as discussed in the main text, is seen in Fig. S4(b).

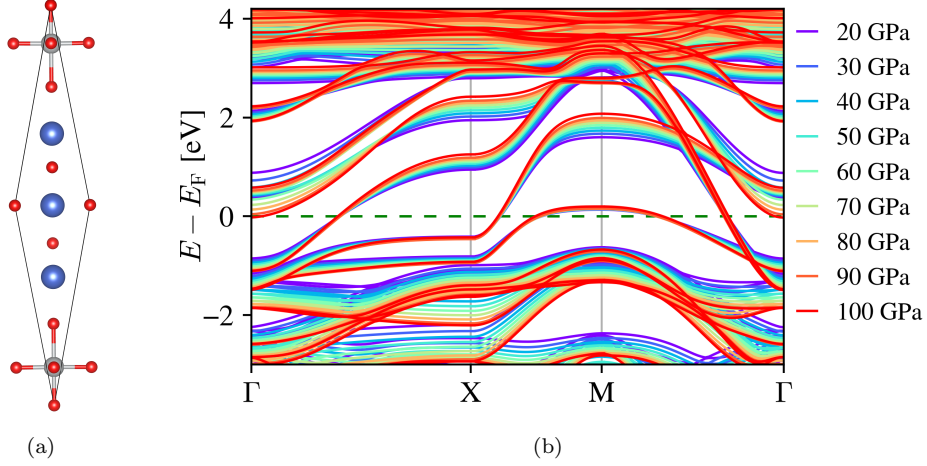


FIG. S4. **Primitive unit cell of bilayer $\text{La}_3\text{Ni}_2\text{O}_7$ in the $I4/mmm$ phase and pressure-dependent band structures.** (a) The crystal structure in the primitive unit cell of the $I4/mmm$ phase containing one structural formula. The atom types are displayed as represented in Fig. S1. (b) DFT band structures at pressures between 20 GPa and 100 GPa.

The character of the bands near E_F can be revealed by projecting the corresponding Kohn-Sham orbitals $\psi_{n\mathbf{k}}$ onto different atomic orbitals centered on the different ion types (represented by spherical harmonics Y_{lm}^α that are non-zero within spheres around a given atom type α). The obtained overlap $|\langle Y_{lm}^\alpha | \psi_{n\mathbf{k}} \rangle|^2$ gives rise to the so-called lm -decomposition of the initial Kohn-Sham states as seen in the PBE band structure at 40 GPa for different atom types α in Fig. S5. The lm -decomposition onto all the atomic orbitals for the target bands around the Fermi level E_F shows by far the strongest character centered on the Ni ions in the middle panel of Fig. S5 and some weak character for the surrounding oxygen centers. The overlap can be divided even more onto the different atomic orbitals labeled by the quantum numbers l and m as seen in Fig. S6.

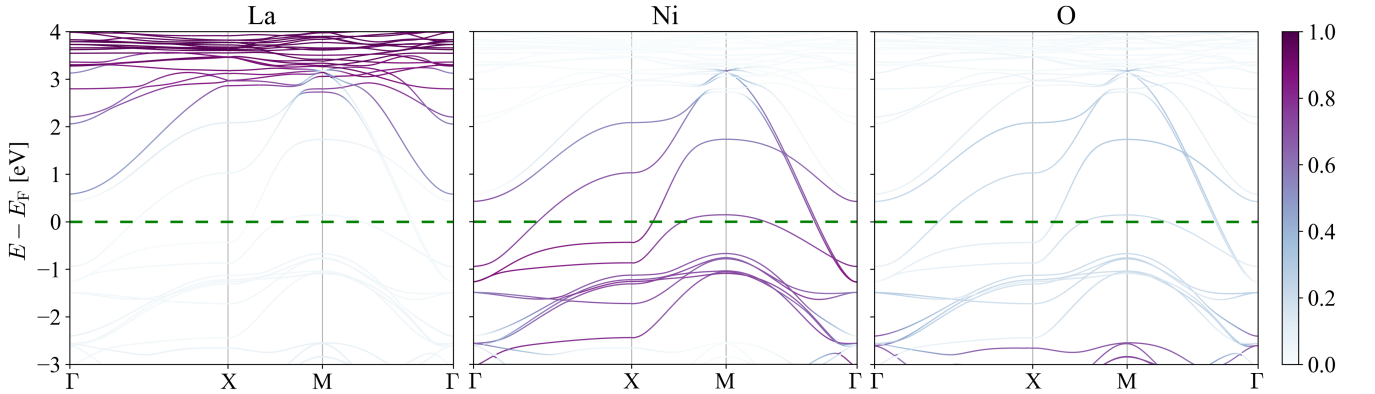


FIG. S5. **The lm -decomposition of bilayer $\text{La}_3\text{Ni}_2\text{O}_7$ at 40 GPa on the different atom types.** The lm -decomposition of the band structure on the different atom types for the range $[-3 \text{ eV}, 4 \text{ eV}]$ relative to the Fermi energy E_F . The color of the band points corresponds to the absolute overlaps $|\langle Y_{lm}^\alpha | \psi_{n\mathbf{k}} \rangle|^2$. In the right figure the contributions of all three (equivalent) oxygen atoms in the unit cell are combined.

The lm -decomposition onto different groups of atomic orbitals as seen in Fig. S6(b-c) reproduces the crystal field splitting of the $3d$ -orbitals into t_{2g} and e_g orbitals under the octahedral geometry. This confirms the presumption of a correlated subspace spanned by the e_g bands and allows, through Wannierization, for a two-dimensional local, effective Hamiltonian as discussed in the main text.

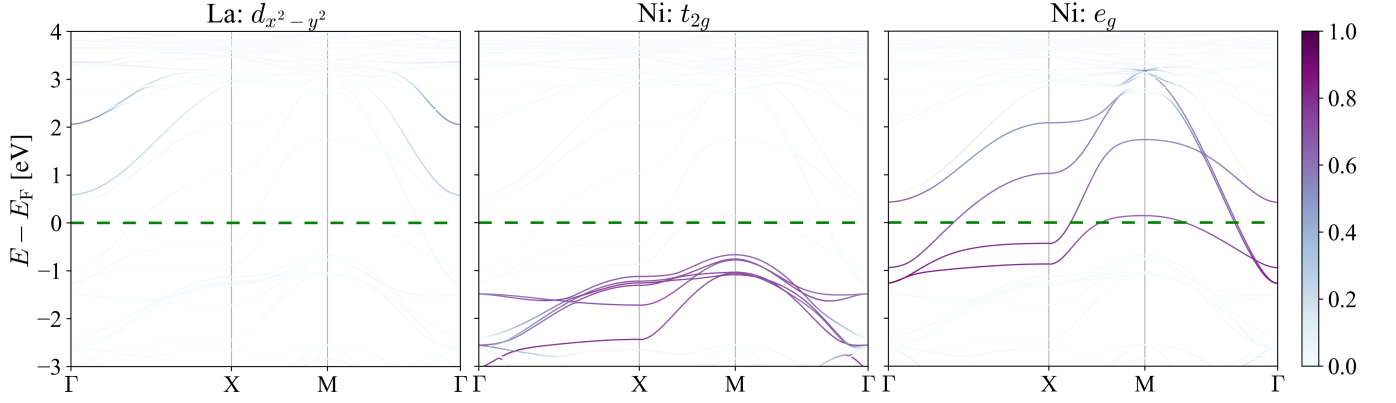


FIG. S6. **The lm -decomposition of bilayer $\text{La}_3\text{Ni}_2\text{O}_7$ at 40 GPa on the different atomic orbitals.** The lm -decomposition of the band structure on (a) the $d_{x^2-y^2}$ orbitals on the La ions, (b) the t_{2g} orbitals of Ni and (c) the e_g orbitals of Ni for the range $[-3 \text{ eV}, 4 \text{ eV}]$ relative to the Fermi energy E_F . The color of the band points corresponds to the absolute overlaps $|\langle Y_{lm}^\alpha | \psi_{n\mathbf{k}} \rangle|^2$.

B. Wannierization

To construct a sufficiently localized basis functions spanning the low-energy subspace, maximally localized Wannier functions (MLWFs) are constructed from the Kohn-Sham orbitals representing the e_g orbitals near E_F . Wannier functions are defined as [68]

$$\phi_{\alpha\mathbf{R}}(\mathbf{r}) = \frac{V}{(2\pi)^3} \int e^{-i\mathbf{k}\cdot\mathbf{R}} \psi_{\alpha\mathbf{k}}^{(w)}(\mathbf{r}) d\mathbf{k}, \quad (1)$$

where the integral is over the first Brillouin zone, V is the real-space primitive cell volume, \mathbf{R} is a real-space lattice vector, and

$$\psi_{\alpha\mathbf{k}}^{(w)}(\mathbf{r}) = \sum_{\beta} T_{\alpha\beta}^{(\mathbf{k})} \psi_{\beta\mathbf{k}}(\mathbf{r}) \quad (2)$$

is a linear combination of Bloch functions $\psi_{\beta\mathbf{k}}(\mathbf{r})$, which are approximated by the Kohn-Sham orbitals. For a discretized Brillouin zone, *i.e.* a set of N_k k -points, as is the case in the reciprocal sampling approach, (1) becomes

$$\phi_{\alpha\mathbf{R}}(\mathbf{r}) = \frac{1}{N_k} \sum_{\beta\mathbf{k}} e^{-i\mathbf{k}\cdot\mathbf{R}} T_{\alpha\beta}^{(\mathbf{k})} \psi_{\beta\mathbf{k}}(\mathbf{r}). \quad (3)$$

The expansion coefficients, $T_{\alpha\beta}^{(\mathbf{k})}$, are uniquely obtained by imposing that the spread,

$$\Omega = \sum_{\alpha} \left(\langle \phi_{\alpha\mathbf{0}} | r^2 | \phi_{\alpha\mathbf{0}} \rangle - \langle \phi_{\alpha\mathbf{0}} | \mathbf{r} | \phi_{\alpha\mathbf{0}} \rangle^2 \right), \quad (4)$$

is minimized, resulting in Wannier functions that are maximally localized in real space.

However, the e_g corresponding to this target state are not isolated from the lower t_{2g} bands and higher La $5d$ bands (see also Fig. S5), so that both the construction of the MLWFs and the screening approach will require disentanglement of these Kohn-Sham bands. The disentanglement scheme of Souza *et al.* [70] initially constructs a set of J smooth Bloch-like states from $\mathcal{J}_{\mathbf{k}} \geq J$ original Bloch bands, where $\mathcal{J}_{\mathbf{k}}$ can vary throughout the first Brillouin zone, and subsequently constructs an orthonormal basis of MLWFs as defined in (1). The $\mathcal{J}_{\mathbf{k}}$ entangled Bloch bands at every calculated point in reciprocal space \mathbf{k} have an energy within the so-called outer energy window, which is fixed by a constant minimum and maximum for the full first Brillouin zone. Within this outer window, an inner window can be defined where the original Bloch states with an energy in this inner window remain unchanged. In this way, $\mathcal{J}_{\mathbf{k}}$ is reduced with the number of original Bloch states in the inner window for every reciprocal point \mathbf{k} . The disentanglement to J Bloch-like states $|\psi_{n\mathbf{k}}\rangle$ is then performed by selecting a set of J localized trial orbitals $g_n(\mathbf{r})$,

which in this case represent the e_g atomic orbitals, and projecting them onto the remaining $\mathcal{J}_{\mathbf{k}}$ original Bloch states $|\psi_{m\mathbf{k}}^0\rangle$,

$$|\psi_{n\mathbf{k}}\rangle = \sum_{m=1}^{\mathcal{J}_{\mathbf{k}}} |\psi_{m\mathbf{k}}^0\rangle \langle \psi_{m\mathbf{k}}^0 | g_n \rangle, \quad (5)$$

which becomes after normalization

$$|\psi_{m\mathbf{k}}^{(w)}\rangle = \sum_{n=1}^J |\psi_{n\mathbf{k}}\rangle (S_{\mathbf{k}}^{-1/2})_{mn} \quad (6)$$

with the normalization matrix $(S_{\mathbf{k}})_{mn} = \langle \psi_{m\mathbf{k}} | \psi_{n\mathbf{k}} \rangle_V = (A_{\mathbf{k}}^\dagger A_{\mathbf{k}})_{mn}$ where $(A_{\mathbf{k}})_{mn} = \langle \psi_{m\mathbf{k}} | g_n \rangle$ is the overlap matrix of dimension $\mathcal{J}_{\mathbf{k}} \times J$.

Given a set of J MLWFs and a Hamiltonian operator \hat{H} , a so-called Wannier interpolation can be done on a denser k -mesh, which requires diagonalisations that are computationally cheap compared to diagonalisations of for example Hamiltonian matrices in the plane wave basis set [78]. The $J \times J$ Hamiltonian matrix in the Wannier gauge can be defined as

$$H_{nm}^{(w)}(\mathbf{q}) = \langle \psi_{n\mathbf{q}}^{(w)} | \hat{H} | \psi_{m\mathbf{q}}^{(w)} \rangle. \quad (7)$$

Transforming this Hamiltonian matrix to real-space using Fourier transform results in

$$H_{nm}^{(w)}(\mathbf{R}) = \frac{1}{N_q^3} \sum_{\mathbf{q}} e^{-i\mathbf{q}\cdot\mathbf{R}} H_{nm}^{(w)}(\mathbf{q}) \quad (8)$$

with N_q the (small) number of reciprocal points used in the calculation of the initial Bloch states. The interpolation to a denser k -mesh can then be done by performing the inverse Fourier transform,

$$H_{nm}^{(w)}(\mathbf{k}) = \sum_{\mathbf{R}} e^{i\mathbf{k}\cdot\mathbf{R}} H_{nm}^{(w)}(\mathbf{R}), \quad (9)$$

on arbitrary k -point \mathbf{k} . The success of this interpolation is due to the localized nature of the MLWFs and thereby of $H_{nm}^{(w)}(\mathbf{R})$. The final step is then to diagonalise $H_{nm}^{(w)}(\mathbf{k})$ to extract the band structure [78]. The discussed MLWF construction en Wannier interpolation of the obtained orbitals is performed with VASP via the Wannier90 interface [55, 56, 69].

As an example of the projected Wannierization and subsequent interpolation, Fig. S7 shows the band structure, disentanglement windows and interpolated bands for $\text{La}_3\text{Ni}_2\text{O}_7$ at 2 GPa ($Cmcm$) and at 40 GPa ($I4/mmm$). For the $Cmcm$ phase, the octahedral tilts entail two major precautions. First of all, the z -orientation of the trial orbitals is not the c -axis, and should be aligned with the out-of-plane Ni-O bonds. Secondly, the resulted angles increased hybridization with other entangled orbitals of no e_g character, which should be maximally excluded as made possible with adequate inner windows. Isosurfaces of the two inequivalent MLWFs per Ni ion can be seen for the crystal structure optimized at 2 GPa in Fig. S7(a), and display strong $d_{x^2-y^2}$ and d_{z^2} character. The individual spreads of each $d_{x^2-y^2}$ and d_{z^2} projected MLWF, as defined in (4), can be seen in Fig. S7(b). In the $Cmcm$ phase (up to approximately 12 GPa), the MLWFs become less localized with increasing octahedral tilt, which impacts the model parameters, as discussed in the main text. All disentanglement windows, relative to E_F , are available from the online GitHub repository.

C. Downfolding

The Kohn-Sham bands are downfolded to the orbital-selective $(2\text{Ni})^{5+}$ dimer configuration, spanned by the e_g MLWFs using the multi-scale *ab initio* scheme for correlated electrons [65, 66]. For bands further away from the Fermi level, it is assumed that correlation is weak and, consequently, that DFT describes the high-energy screening adequately. When a suitable low-energy space is obtained, the most important parameters defining a effective multi-band Hubbard model can be obtained. In many-body perturbation theory, the random phase approximation is used to typically used to approximate the screened interaction in function of the bare interaction v as

$$W = \frac{v}{1 - vP}. \quad (10)$$

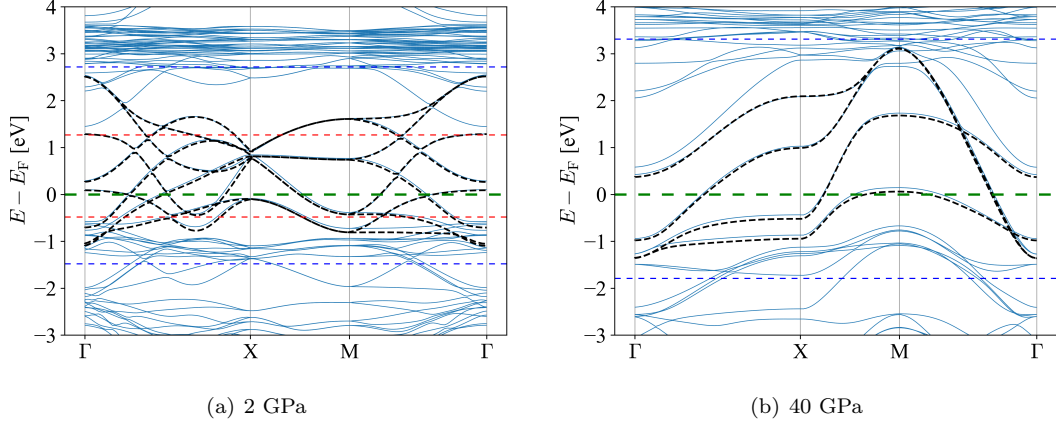


FIG. S7. **Wannier interpolated band structures in both low-temperature phases of bilayer $\text{La}_3\text{Ni}_2\text{O}_7$.** PBE band structure for the crystal structures optimized at (a) 2 GPa in the $Cmcm$ phase and (b) 40 GPa in the $I4/mmm$ phase, shown as solid blue lines. The outer- and, for the $Cmcm$ phase, inner disentanglement windows are given as blue and red horizontal lines. The Wannier-interpolated bands of the MLWFs, constructed by projecting the PBE bands onto these e_g orbitals, are shown as dashed lines.

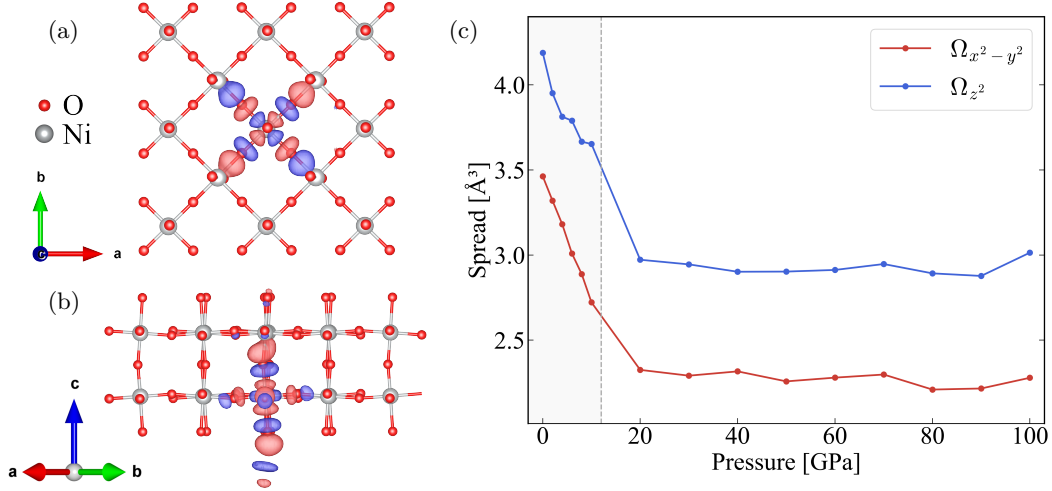


FIG. S8. **Maximally localized Wannier functions of bilayer $\text{La}_3\text{Ni}_2\text{O}_7$.** The isosurface plots of the MLWFs centered on a Ni ion and projected on the (a) $d_{x^2-y^2}$ and (b) d_{z^2} orbitals. (c) The corresponding spreads as defined in (4), respectively, for the crystal structure of $\text{La}_3\text{Ni}_2\text{O}_7$ optimized at 2 GPa.

The polarization function in the frequency domain is then given by

$$P(\mathbf{r}, \mathbf{r}', \omega) = - \sum_{\alpha\mathbf{k}}^{\text{occ}} \sum_{\alpha'\mathbf{k}'}^{\text{unocc}} \frac{\psi_{\alpha\mathbf{k}}(\mathbf{r}) \psi_{\alpha'\mathbf{k}'}^*(\mathbf{r}) \psi_{\alpha'\mathbf{k}'}(\mathbf{r}') \psi_{\alpha\mathbf{k}}^*(\mathbf{r}')}{\omega + \varepsilon_{\alpha'\mathbf{k}'} - \varepsilon_{\alpha\mathbf{k}} - i\eta} + \sum_{\alpha\mathbf{k}}^{\text{occ}} \sum_{\alpha'\mathbf{k}'}^{\text{unocc}} \frac{\psi_{\alpha\mathbf{k}}^*(\mathbf{r}) \psi_{\alpha'\mathbf{k}'}(\mathbf{r}) \psi_{\alpha'\mathbf{k}'}^*(\mathbf{r}') \psi_{\alpha\mathbf{k}}(\mathbf{r}')}{\omega - \varepsilon_{\alpha'\mathbf{k}'} + \varepsilon_{\alpha\mathbf{k}} + i\eta}$$

with $\varepsilon_{\alpha\mathbf{k}}$ the eigenvalue corresponding to orbital $\psi_{\alpha\mathbf{k}}(\mathbf{r})$ and η an infinitesimally small positive number. The summations over the occupied and unoccupied states can be interpreted as a summation over all possible transitions from below the Fermi energy to above.

The main idea of the constrained random phase approximation (cRPA) is then to split this sum into the transitions within the chosen low-energy subspace and the remaining transitions, $P = P_l + P_r$. As the screening due to states within the target space is included in the effective model, we exclude them from the screened interaction to arrive at a partially screened interaction

$$W_r = \frac{v}{1 - vP_r}, \quad (11)$$

which is to be identified with the Hubbard U . However, separating the sum into P_l and P_r is not trivial when the bands of the two subspaces are entangled with each other. Similar to the disentanglement of the Kohn-Sham bands for the Wannierization in (6), the projector method [67] initially projects both wave functions on the propagators in (11) individually. The polarization function within the low-energy subspace then becomes

$$P_l(\mathbf{r}, \mathbf{r}', \omega) = \sum_m \sum_{m'}^{occ \ unocc} A_{mm'}(\mathbf{r}) \times B_{mm'}(\mathbf{r}') \left[\frac{1}{\omega - \epsilon_{m'} + \epsilon_m + i\eta} - \frac{1}{\omega + \epsilon_{m'} - \epsilon_m - i\eta} \right] \quad (12)$$

with the projected products A and B defined as

$$A_{mm'}(\mathbf{r}) = \sum_{m_1, m'_2} \mathcal{P}_{m_1 m}^* \psi_{m_1}^*(\mathbf{r}) \psi_{m'_2}(\mathbf{r}) \mathcal{P}_{m'_2 m'} \quad (13)$$

$$B_{mm'}(\mathbf{r}) = \sum_{m'_1, m_2} \mathcal{P}_{m_2 m'}^* \psi_{m_2}^*(\mathbf{r}) \psi_{m'_1}(\mathbf{r}) \mathcal{P}_{m'_1 m} \quad (14)$$

and the target projectors \mathcal{P}_{mn} defined as

$$\mathcal{P}_{mn} = \sum_l \langle \phi_l | \psi_m \rangle \langle \psi_n | \phi_l \rangle. \quad (15)$$

These projectors \mathcal{P}_{mn} map the initial, entangled wave functions $\psi_m(\mathbf{r})$ to a new set of states $\psi_n(\mathbf{r})$, with expansion coefficients being the overlap with the MLWFs spanning the low-energy subspace. The projected products A and B therefore filter out relative contributions of the low-energy subspace to every initial wave function ψ_m .

The dimer model parameters (both the effective interactions and hopping integrals) are obtained by presenting the effective one- and two-body Hamiltonians in the obtained MLWF basis. Presenting the screened Coulomb interaction in this basis gives rise to the following interaction parameters:

$$U_{\mathbf{R}_i i, \mathbf{R}_i i'; \mathbf{R}_j j, \mathbf{R}_j j'}(\omega) = \int \int d^3 r d^3 r' \phi_{i\mathbf{R}_i}^*(\mathbf{r}) \phi_{j\mathbf{R}_j}^*(\mathbf{r}') \hat{\mathcal{H}}_U \phi_{i'\mathbf{R}_i'}(\mathbf{r}) \phi_{j'\mathbf{R}_j'}(\mathbf{r}'), \quad (16)$$

where the effective interaction Hamiltonian $\hat{\mathcal{H}}_U$ is the effective Coulomb interaction $W_r(\mathbf{r}, \mathbf{r}', \omega)$ in (11). The hopping terms (*i.e.* the kinetic terms) can be obtained similarly by presenting the effective one-body Hamiltonian $\hat{\mathcal{H}}_K$ in the MLWF basis:

$$t_{\mathbf{R}_i \mathbf{R}_i'} = - \int d\mathbf{r} \phi_{i\mathbf{R}_i}^*(\mathbf{r}) \hat{H}_K^{KS} \phi_{i'\mathbf{R}_i'}(\mathbf{r}). \quad (17)$$

The cRPA screening and subsequent Hubbard interaction terms are computed completely within the VASP software, while the hopping integrals are obtained from post-processing hopping code as given in the online GitHub repository [55, 56].

Although frequency dependence can have non-negligible effects, the parameters are chosen to be static, $\omega = 0$. This can be justified by the retarded screening effects being negligible for small ω , as seen by the horizontal slopes of the on-site Hubbard interactions of $\text{La}_3\text{Ni}_2\text{O}_7$ at 40 and 70 GPa in Fig. S9.

Fig. S10(a) shows the lm -decomposed band structure of bilayer $\text{Ac}_3\text{Ni}_2\text{O}_7$ at 4 GPa, *i.e.* projected onto the Ni e_g orbitals. The projection onto the Ac $d_{x^2-y^2}$ is superimposed as purple circles, with radii representing the absolute overlap value. The four lowest-energy bands clearly exhibit e_g character, with the different contributions varying significantly across the Brillouin zone.

S3. AB INITIO MOLECULAR DYNAMICS

In our *ab initio* molecular dynamics (AIMD) simulations, we employed the Nosé-Hoover thermostat and the Parrinello-Rahman barostat to ensure the isoenthalpic-isobaric ensemble, where both atomic positions and cell parameters (volume and shape) are allowed to evolve during the simulation [60–64]. Fig. S11 shows the time-averaged values of pressure (derived from atomic forces) and temperature (derived from atomic velocities) during the NPT AIMD simulation. These results confirm the proper implementation of both the thermostat and barostat settings over the full simulation regime, ensuring the system is in a stable ensemble.

Finally, as a more quantitative evidence of the thermal spread of the interlayer angle θ_1 and absolute difference in the basal angle θ_2 within the $I4/mmm$ phase in Fig. 4, the frequency histograms are given for four points within this phase in Fig. S12.

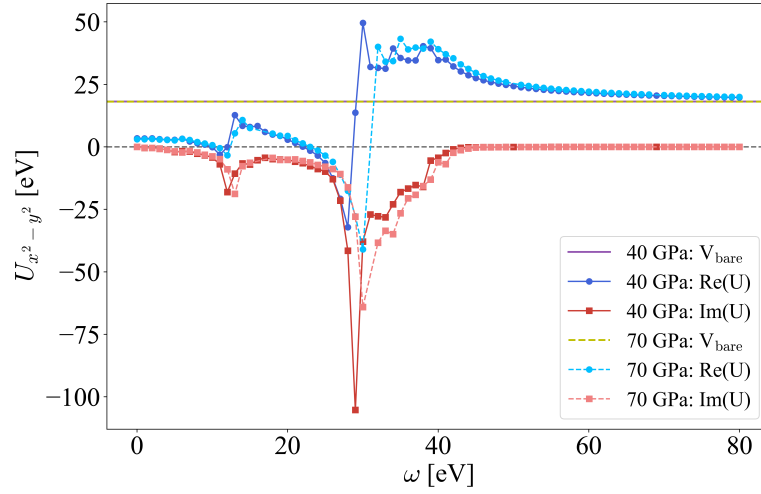


FIG. S9. **Frequency dependence of cRPA screening in bilayer $\text{La}_3\text{Ni}_2\text{O}_7$.** Frequency dependence of the real and imaginary part of the on-site screened Coulomb interaction $U_{d_{x^2-y^2}}$ of bilayer $\text{La}_3\text{Ni}_2\text{O}_7$ optimized at 40 and 70 GPa.

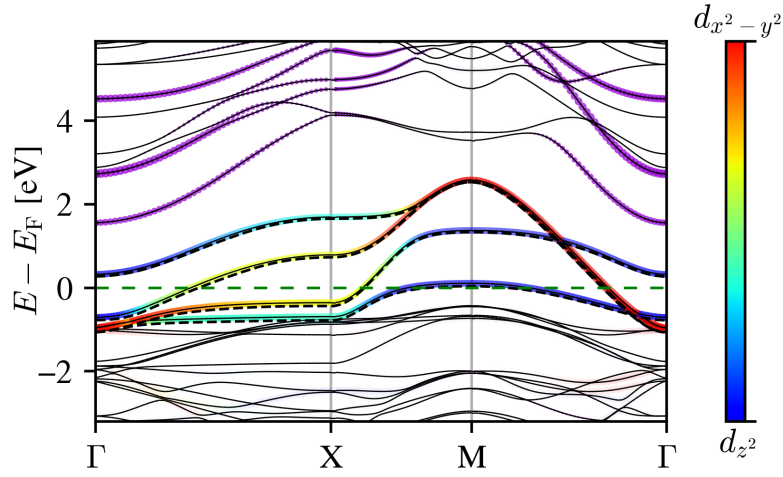


FIG. S10. **Band structure and MLWFs of bilayer $\text{Ac}_3\text{Ni}_2\text{O}_7$.** (a) Band structure at 4 GPa, shown as solid black lines, with the superimposed color scale indicating the relative lm -projected weight of the different Ni e_g orbitals. The projection onto the Ac $d_{x^2-y^2}$ is superimposed as purple circles, with radii representing the corresponding weight. The Wannier-interpolated bands obtained from the MLWFs are shown as dashed lines.

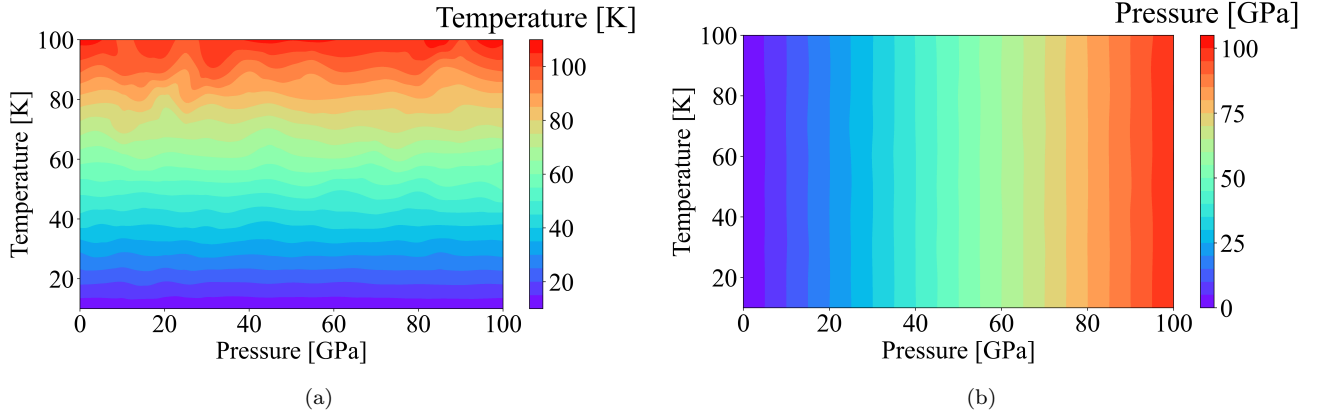


FIG. S11. **Confirmation ensemble stability of the AIMD simulations.** The averaged (a) temperature and (b) pressure as measured from the AIMD trajectories in the temperature-pressure phase diagram of bilayer $\text{La}_3\text{Ni}_2\text{O}_7$ in the range of 10–100 K and 0–100 GPa through AIMD simulations.

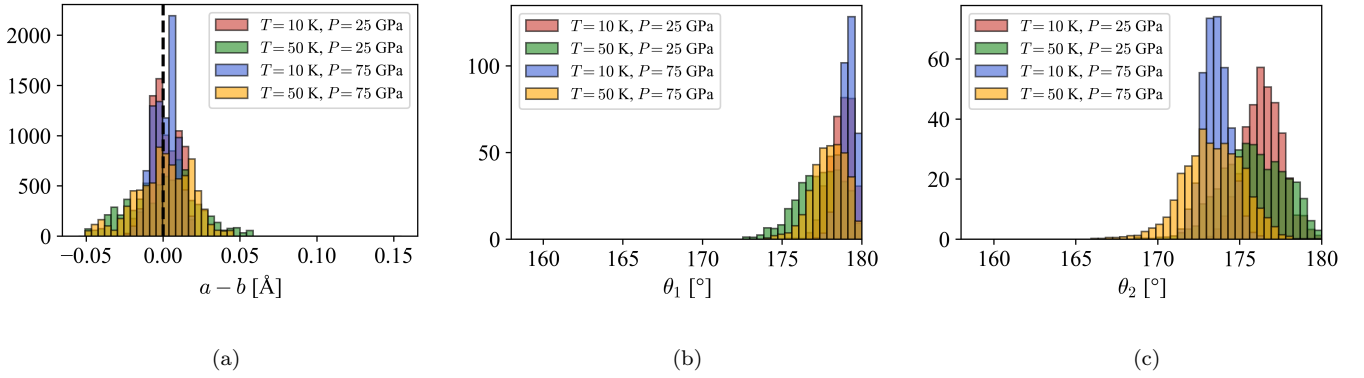


FIG. S12. **Frequency histograms in the $I4/mmm$ phase.** Frequency histograms at four indicated pressure-temperature points in the $I4/mmm$ phase, showing the increased thermal fluctuations and pressure-driven basal folding.